主办 中国科学院遥感与数字地球研究所
中国地理学会环境遥感分会
出版 科学出版社

JOURNAL OF REMOTE SENSING

遥感学报

2013年 Vol.17 第17卷 No.4 第4期 ISSN 1007-4619 CN11-3841 / TP CODEN YXAUAB

2010年中国土地覆被遥感监测数据集（ChinaCover2010）

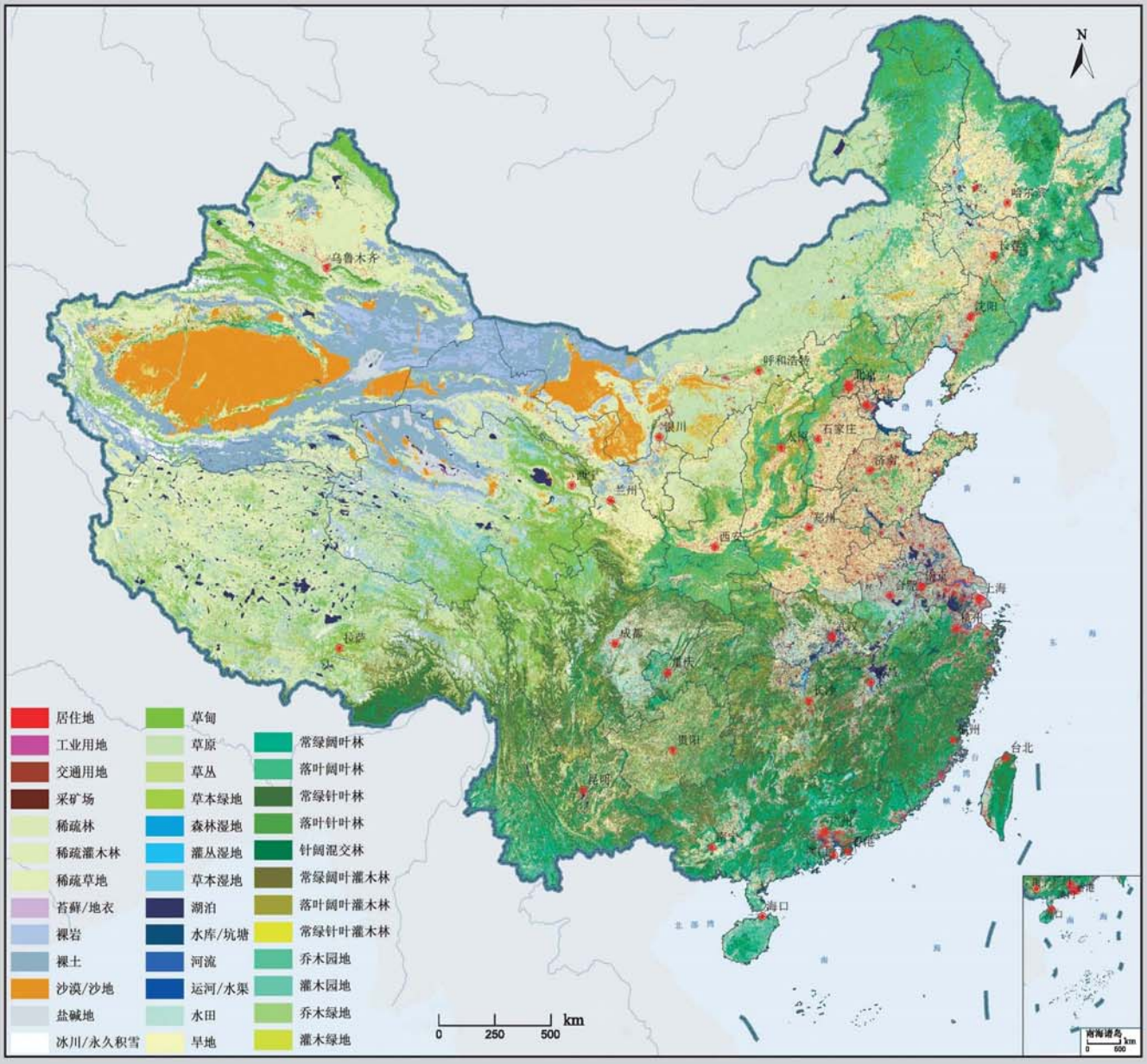

百种中国杰出学术期刊

遥感学报

Yaogan Xuebao

第 17 卷　　第 4 期　　2013 年 7 月

目　　次

JOURNAL OF REMOTE SENSING

(Vol. 17 No. 4 July, 2013)

CONTENTS

(to be continued to Inside Back Cover)

(continued from Contents page)

Haze: Remote Sensing

Atmospheric correction of MERIS data on the black pixel assumption in oxygen and water vapor absorption bands

TAN Jing[1], LI Yunmei[1], Zhao Yunlin[2], LV Heng[1], XU Deqiang[3], ZHOU Li[1], LIU Ge[1]

1. *Key Laboratory of Virtual Geographic Environment Ministry of Education*, *Nanjing Normal University*, *Nanjing* 210046, *China*;
2. *Hunan City University*, *Yiyang* 413000, *China*;
3. *Yixing Hydrological Water Resources Monitoring Center*, *Yixing* 214200, *China*

Abstract: A Medium-Resolution Imaging Spectrometer (MERIS) sensor, with reasonable ocean color bands and a high spatial resolution of 300 m, has considerable potential with respect to the monitoring of inland waters. In the quantitative retrieval of water environmental parameters by using a remote sensing image, accurate atmospheric correction is very significant. In the present study, oxygen and water vapor absorption bands are used for improving the traditional black pixel assumption based on the near-infrared bands. The method of calculating aerosol parameters through MERIS Level 2p data is developed; this method is assessed using MERIS Level 1p data recorded on Nov. 11, 2007; Nov. 20, 2008; and April 25, 2009. Meanwhile, the *in situ* measured data are used for a comparison with the modeled values. The obtained results show that the proposed method is efficacious with RMSP of less than 25%. Another important work is also carried out, that is, a comparison of the proposed method with other algorithms such as a case II atmospheric correction algorithm embedded in a MERIS (Beam) processor, aerosol-thickness-aided 6S, and modified black pixel algorithm. The results indicate that the proposed algorithm has certain applicability considering, because it is independent of the synchronous measured aerosol data.

Key words: atmospheric correction, MERIS data, case II water, absorption bands

CLC number: TP751 **Document code**: A

Citation format: **Tan J, Li Y M, Zhao Y L, Lv H, Xu D Q, Zhou L and Liu G. 2013. Atmospheric correction of MERIS data on the black pixel assumption in oxygen and water vapor absorption bands. Journal of Remote Sensing, 17(4): 768-787** [**DOI: 10.11834/jrs.20132102**]

1 INTRODUCTION

Among the Top-of-Atmosphere (TOA) radiance, there is only a 10% transfer from the water in the visible spectrum (Huot, et al., 2001). Atmospheric scattering information causes significant interference in the water spectral information, which in turn seriously affects the extraction of water quality parameters. Consequently, atmospheric correction is critical for an accurate retrieval of water leaving reflectance and alleviation of atmospheric contaminations in order to improve the accuracy of the remote sensing monitoring of water environment. Theoretically, an atmospheric signal is mainly made of Rayleigh scattering by gas molecules, Mie scattering by aerosols, and their interaction. Because of its stable molecular composition and content, Rayleigh scattering can be exactly calculated from radiative transfer models considering multiple scattering and polarization (Gordon, et al., 1988; He, et al., 2007) and predicted *a priori*, while aerosol scattering, because of its considerable changes in space and time, remains the largest uncertainty in the retrieval of water-leaving reflectance, which is the core of different atmospheric correction algorithms.

The traditional method for retrieving aerosol scattering is also known as the black pixel assumption method; in this method, water-leaving reflectance is assumed to approach zero at a Near Infrared (NIR) wavelength (>700 nm). With this black pixel assumption, the aerosol scattering at two NIR wavelengths can be derived and extrapolated to the visible wavelengths on the basis of the property of aerosol wavelength dependence (Richard, et al., 1999), and then, the atmospheric contribution can be subtracted from the TOA signal (this method is also called the standard NIR algorithm). However, for case II waters such as coastal areas and inland lakes, this assumption is invalid because of the high reflection by suspended particles in the NIR bands (the optical characteristics of case I waters are mainly determined by phytoplankton and its concomitant, such as the open ocean water, while the optical characteristics of case II waters are mainly determined by the suspended particles and Colored Dissolved Organic Matter (CDOM); inland and coastal waters

Received: 2012-03-28; **Accepted**: 2012-10-05; **Version of record first published**: 2012-10-13

Foundation: National Natural Science Foundation of China (No. 40971215);The Special Foundation of Environmental Nonprofit Industry Research of China (No. 2010467022); The major projects of natural science research of Jiangsu province universities (No.11KJA170003)

First author biography: TAN Jing (1987—), female, master candidate, she majors in GIS and remote sensing of environment. E-mail: tanjing871015@163.com

Corresponding author biography: Li Yunmei (1966—), female, professor,her research interest is remote sensing of environment. E-mail: liyunmei@njnu.edu.cn

that are seriously affected by terrigenous substance emissions are of the latter type (Zhang, et al., 2008; Yang, et al., 2008; David, et al., 2000).

Hu, et al. (2000) proposed an atmospheric correction algorithm on the basis of the abovementioned case I water atmospheric correction algorithm. The algorithm assumes that the aerosol type remains stable within a small space range (approximately 50 km to 100 km); hence, we can obtain the aerosol type parameter from the clean water using the original standard NIR algorithm and then pass this parameter to the surrounding turbid regions. Ruddick, et al. (2000) put forward two assumptions: (1) the ratio of aerosol multiple scattering reflectance of the 765 nm and 865 nm bands remains unchanged in the study area; and (2) the ratio of seawater reflectance of the 765 nm and 865 nm bands corrected by atmospheric diffuse transmittance T_0 (from the sun to the surface) remains unchanged. Then, we solve the simultaneous equations to obtain the NIR water leaving reflectance under the above assumptions. Kuchinke, et al. (2009) established the spectrum optimization algorithm for case II waters in order to calculate the aerosol reflectance combined with the biological optical model and the aerosol model (using the Junge spectrum description). Wang, et al. (2007) attempted to overcome the non-black fact at NIR bands by using Shor Twave Infrared Bands (SWIR) of MODIS data, regarding the water leaving reflectance in these bands as negligible because of its strong absorption, and obtained a better correction effect.

With respect to the MERIS data, because of the shortage of SWIR bands, the NIR/SWIR algorithm cannot be extended to the MERIS data directly. For this reason, the Neural Network (NN) inversion algorithm, namely MERIS Regional Case 2 Water Algorithm (C2R), has been proposed and implemented in the MERIS lake water processors Beam 4.8 (Roland, et al., 2008). On the other hand, Huang, et al. (2011) proposed a modified algorithm for the MERIS data. They obtained an error within the acceptable range using the atmospheric correction and successfully sampled the MERIS Level 2p data to amend the atmospheric path radiation of the MERIS Level 1p data.

Zhu, et al. (2012) developed an alternative NIR atmospheric correction algorithm for the MERIS data over inland case II waters by replacing the traditional NIR bands by two specific bands: the oxygen absorption band of 761 nm and the water vapor absorption band of 900 nm so as to keep the assumption of zero water leaving of the chosen black pixels and obtained a better correction accuracy. In this paper, we used the MERIS Level 2p product to assist the dark pixel selection and made improvements to the abovementioned algorithm. At the same time, we compared the accuracy of this method with that of the Beam C2R algorithm, the aerosol-thickness-aided 6S algorithm, and the modified black pixel algorithm.

2 STUDY AREA AND DATA

2.1 Overview of study area

Taihu lake is one of the five largest freshwater lakes in China with the area of 2427.8 km^2 and the average depth of 1.9 m. The actual surface area of water is 2338.1 km^2 because there are 51 central islands. With its lake strandline presidents to 405 km, Taihu lake is a typical large shallow inland lake (Sun et al., 1993; Li et al., 2008). The latitude and longitude range of Taihu lake is between 30°55′40″—31°32′58″N and 119°52′32″—120°36′10″E. The west, the north, and the southeast boundaries of Taihu lake are Changzhou city, Wuxi city, and Suzhou city of Jiangsu province, respectively. The south and the southwest boundaries of Taihu lake are Huzhou city and Changxing county, respectively. Taihu lake is located in the inland-developed urban agglomerations of the Yangtze River Delta; therefore, the water quality is significantly affected by terrigenous emissions as well as human activities. Water optical properties are complex and changeable, jointly decided by chlorophyll, suspended matter, and CDOM, revealing typical case II water characteristics (Zhang, et al., 2008).

2.2 Data and processing

2.2.1 *Image data and preprocessing*

Three full-resolution (300 m) Medium-Resolution Imaging Spectrometer (MERIS) images (MERIS Level 1p and MERIS Level 2p) covering Taihu lake were acquired on Nov. 11, 2007, Nov. 20, 2008, and April 25, 2009. The MERIS onboard Europe satellite agency Environmental Satellite (ENVISAT) was launched on March 1, 2002 and is mainly used for marine and coastal ocean color monitoring. The MERIS Level 1p data are the TOA reflectance after the radiometric calibration processing of the Digital Number (DN) value, while the MERIS Level 2p data are the result of the atmospheric correction of MERIS Level 1p data by its own algorithm. MERIS has a narrower band-setting than the Sea-viewing Wide Field-of-View Sensor (SeaWiFS) and the Moderate Resolution Imaging Spectroradiometer (MODIS). In addition to the conventional atmospheric correction bands, band 12 and band 14 are located at the central wavelengths of 778.75 nm and 885 nm with the band width of 15 nm and 10 nm, respectively. The sensor also has specific oxygen and water vapor absorption bands with a central wavelength of 760.16 nm and 900 nm and a bandwidth of 3.75 nm and 10 nm, respectively.

The overlapping phenomenon of the MERIS Level 1p data was removed using the smile correction processor provided by Beam 4.8. Thereafter, the corrected radiance was converted to reflectance in order to obtain the dimensionless value by using Eq.(1) (Gordon & Wang, 1994a)

$$\rho = \pi L / F_0 \cos\theta_0 \quad (1)$$

where ρ, L, F_0, and θ_0 represent the TOA reflectance, the TOA radiance, the TOA irradiance, and the solar zenith angle, respectively.

2.2.2 *In situ data*

Three field campaigns were undertaken in Taihu lake on Nov.11, 2007, Nov. 20, 2008, and April 25, 2009, and the remote sensing reflectance (R_{rs}) data of the field samples were acquired. The samples, as well as the depth distribution of Taihu lake, are shown in Fig.1.

Hyper-spectral reflectance measurements were recorded using an ASD Field Spec spectroradiometer. Spectral radiance was measured at 2 nm intervals from 350 nm to 1050 nm.

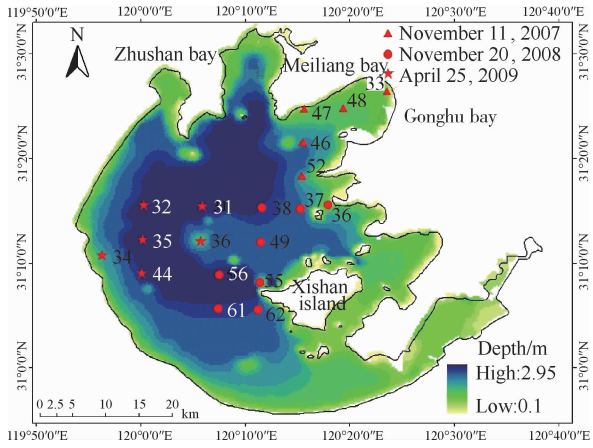

Fig.1 Distribution of sample sites and depth in Taihu lake

During the measurements, the instrument was held over the deck of an anchored ship approximately 1 m above the water surface according to the method proposed by Tang, et al. (2004). Radiance was measured for the water surface, sky, and a 30% gray board. Ten curves were acquired for each target, and at the same time, the GPS coordinates, the wind speed and direction, and the time information were also recorded. Then, the remote sensing reflectance (R_{rs}) was extracted using Eq.(2)

$$R_{rs} = \frac{(L_{sw} - rL_{sky}) \cdot \rho_p}{L_p \pi} \quad (2)$$

where R_{rs}, L_{sw}, L_{sky}, L_p, and ρ_p are the remote sensing reflectance, the total radiance, the sky diffuse scattering radiance, and the radiance and the reflectance of the gray board, respectively. The value of r is 0.025 (Tang, et al., 2004).

3 ATMOSPHERIC CORRECTION ALGORITHM BASED ON THE BLACK PIXEL ASSUMPTION IN OXYGEN AND WATER VAPOR ABSORPTION BANDS

3.1 Traditional NIR/SWIR method

Typically, the satellite-sensed reflectance, $\rho_t(\lambda)$, is determined by the reflectance of atmospheric components according to distinct physical processes as Eq.(3),

$$\rho_t(\lambda) = \rho_r(\lambda) + \rho_a(\lambda) + T\rho_g(\lambda) + t\rho_{wc}(\lambda) + t\rho_w(\lambda) + t\rho_b(\lambda) \quad (3)$$

where $\rho_r(\lambda)$, $\rho_a(\lambda)$, $\rho_g(\lambda)$, $\rho_{wc}(\lambda)$, and $\rho_b(\lambda)$ represent the contributions of Rayleigh scattering, aerosols scattering, sun glitter off the water surface, water whitecap, and bottom material, respectively. $\rho_w(\lambda)$ is the water leaving reflectance, that is, the desired quantity in water remote sensing. T and t represent the direct and diffuse transmittances of the atmospheric column, respectively.

In Eq.(3), the contribution of sun glitter $\rho_g(\lambda)$ can be ignored when the image data are continuous and stable without any mutation value. Further, the contribution of the bottom material can also be ignored since it can hardly transmit to the surface in turbid waters. The $\rho_{wc}(\lambda)$ term is also not considered when the wind speed is less than 4 m/s. Even more, when the wind speed is between 4 m/s and 7 m/s, it also can be negligible because its order of magnitude is 10^{-4}, which is far less than 10^{-2}, that of reflectance. Under the calm water surface assumption, the $\rho_{wc}(\lambda)$ term is also not considered for the sake of simplicity (Gordon & Wang, 1994b). Accordingly, Eq.(3) can be rewritten below.

$$\rho_t(\lambda) = \rho_r(\lambda) + \rho_a(\lambda) + t\rho_w(\lambda) \quad (4)$$

The diffuse transmittance of the atmospheric column t, mainly influenced by molecular scattering and ozone absorption, can also be calculated approximately by using the following equation (Siegel, 2000),

$$t = \exp(-(\tau_r/2 + \tau_{OZ})/\cos\theta) \quad (5)$$

where τ_r and τ_{OZ} are the Rayleigh optical thickness and the ozone optical thickness, respectively, and θ is the view zenith angle.

Usually, the Rayleigh scattering reflectance, $\rho_r(\lambda)$, can be exactly computed by solving the radiative transfer equations (He, 2007). Then, the rest signal $\rho_c(\lambda)$ is only contributed by the aerosol scattering and the water-leaving reflectance.

$$\rho_c(\lambda) = \rho_a(\lambda) + t\rho_w(\lambda) \quad (6)$$

Thereafter, only the contribution from scattering by aerosol, $\rho_a(\lambda)$, is unknown in Eq.(6). As the aerosol model and concentration are highly variable in the spatial and temporal domains, $\rho_a(\lambda)$ cannot be predicted *a priori* like the Rayleigh scattering. The estimation of the aerosol component, $\rho_a(\lambda)$, becomes a key problem of atmospheric correction. Under the condition of aerosol single-scattering, the contribution of the aerosol component can be written below,

$$\rho_a(\lambda) = \rho_{as}(\lambda) = \omega_a(\lambda)\tau_a(\lambda)p_a(\theta,\theta_0,\lambda)/4\cos\theta\cos\theta_0 \quad (7)$$

where $\rho_{as}(\lambda)$ represents the single scattering reflectance; ω_a, τ_a, and P_a are the aerosol optical thickness, the aerosol single-scattering albedo, and the aerosol scattering phase function, respectively, for a scattering angle and wavelength. According to Wang & Gordon (1994), the atmospheric correction parameter, $\varepsilon(\lambda_i, \lambda_j)$ can be defined as Eq.(8),

$$\varepsilon(\lambda_i,\lambda_j) = \frac{\rho_{as}(\lambda_i)}{\rho_{as}(\lambda_j)} = \frac{\omega_a(\lambda_i)\tau_a(\lambda_i)P_a(\theta,\theta_0,\lambda_i)}{\omega_a(\lambda_j)\tau_a(\lambda_j)P_a(\theta,\theta_0,\lambda_j)} \quad (8)$$

where λ_i and λ_j are the shorter and the longer wavelength, respectively. For the same type of aerosol model, ω_a can be considered to be a fixed value, while the aerosol scattering phase function P_a is a function of the observation geometry and wavelength. The ratio of P_a can also be considered to be constant because of a large number of statistical researches. The aerosol optical thickness, $\tau_a(\lambda)$, dependent on the wavelength (Ångström, 1929), can be estimated as

$$\tau_a(\lambda) = \sigma\lambda^{-\beta} \quad (9)$$

where σ and β are the Ångström exponent and the air turbidity index, respectively, which are constant for a certain aerosol model. Accordingly, Eq.(8) can be simplified below.

$$\varepsilon(\lambda_i,\lambda_j) = \frac{\rho_{as}(\lambda_i)}{\rho_{as}(\lambda_j)} = \frac{\tau_a(\lambda_i)}{\tau_a(\lambda_j)} = \left(\frac{\lambda_j}{\lambda_i}\right)^n \quad (10)$$

Wang & Gordon (1994) proposed another method to calculate $\varepsilon(\lambda_i,\lambda_{NIR})$ (i.e., Eq.(11)), on the basis of a large number of aerosol model simulation results, which is considered to be more accurate.

$$\varepsilon(\lambda_i,\lambda_{NIR}) = \frac{\rho_{as}(\lambda_i)}{\rho_{as}(\lambda_{NIR})} = \exp(C(\lambda_{NIR} - \lambda_i)) \quad (11)$$

where C, under a certain aerosol model, is a constant like n in Eq.(10). The water leaving reflectance of clean water pixels

approaches zero because of its strong absorption in the NIR/SWIR bands; therefore, we can derive the contribution of aerosols from Eq.(6). On the other hand, the atmospheric correction parameter of the NIR/SWIR bands, $\varepsilon(\lambda_i, \lambda_j)$, can be calculated and derived to the full wavelength from Eq.(11) or Eq.(12). In this case, the water-leaving reflectance in the visible bands can also be derived from Eq. (6). Thus far, the entire atmospheric correction process is completed. Otherwise, in the case of Taihu lake, since the lake has a large area of 2427.8 km^2, the spatial distribution of the aerosol is not necessarily uniform. In contrast, the determination of the aerosol model of the entire area just by using a single dark pixel might cause a certain degree of error. Therefore, some further improvements on the issue of clean water pixel selection are required.

3.2 Improved atmospheric correction algorithm against MERIS data

To use the MERIS data, researchers are focusing on the determination of the aerosol model of the study area because of the lack of SWIR bands. Although the MERIS has two conventional atmospheric correction NIR bands, because of the high reflectance of the turbid water in the study area, the assumption that the water leaving reflectance approaches zero cannot be established. Instead, the sensor is equipped with two oxygen and water-vapor absorption bands, i.e., 761 nm and 900 nm, which establishes the assumption. Therefore, we assumed that the traditional NIR/SWIR algorithm could be improved using these two specific bands.

3.2.1 Dark pixel selection using MERIS Level 2p data as auxiliary

The MERIS Level 2p data are a product of the atmospheric correction of the MERIS Level 1p data. The process is as below: First, the water leaving reflectance is obtained through the embedded look-up table with an assumed initial value of the concentration of the suspended particles. Thereafter, the atmospheric correction is conducted with iterative optimization using Gordon's atmospheric correction method considering the relationship between the water leaving reflectance and the inherent optical properties in the NIR bands (Moore, 1999).

The above-mentioned method is efficacious in case I waters, as well as in case II inshore waters, where the concentration of suspended particles and CDOM are relatively low. However, in the case of inland turbid waters, the method still has certain limitations (Huang, et al., 2011) with the excessive correction phenomenon often appearing in the short-wave visible bands, in which the water leaving reflectance is always less than zero except for a few areas with low turbidity.

As compared to those of the open ocean waters, the components of water in Taihu Lake are more complex: the optical characteristics of water are affected by the algae combined with the high concentration of suspended matter and CDOM. As shown in the true color image of Taihu Lake on November.11, 2007 (Fig. 2), the relatively high concentration of the suspended matter leads to the tawny rendering in the central and southwest regions of the study area. The blue-green color in Zhushan Bay, Gonghu Bay, Xukou Bay, and the East Taihu Lake depicts a low concentration of the suspended matter. According to previous research, there are many aquatic plants in Eastern Taihu Lake making it relatively clean, which is consistent with the blue-green area in the true-color image.

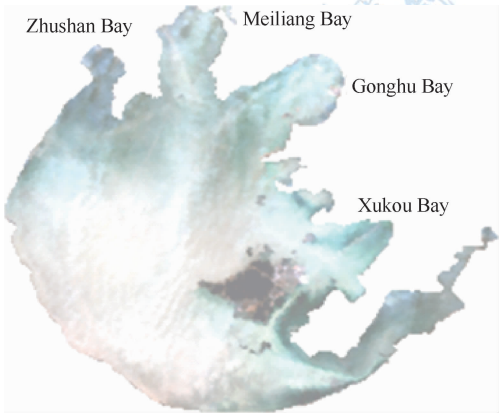

Fig.2 True color image of band 6, band 4, and band 2 recorded on November 11, 2007

The pixels with water leaving reflectance larger than zero at 412 nm were relatively rare (Fig. 3), were mostly located in East Taihu lake and Xukou Bay, and sporadically distributed at the entrance of Zhushan Bay and Gonghu Bay. Therefore, the dark pixels were selected as relatively clean water. The distribution of these dark pixels is consistent with the information reflected in Fig.2, which could be further used for a subsequent dark pixel selection.

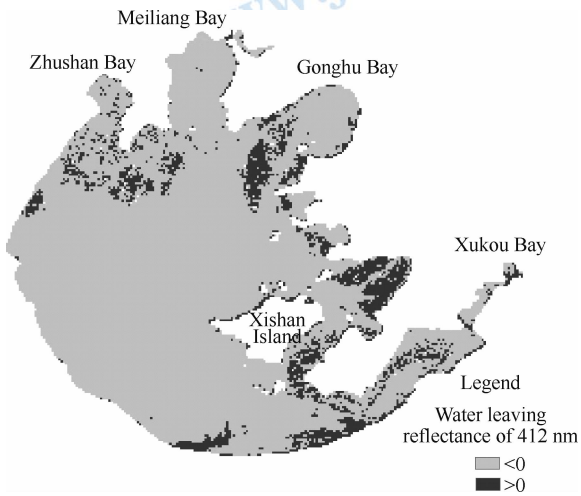

Fig.3 Water leaving reflectance of 412 nm band of MERIS Level 2p data recorded on November.11, 2007

Multiple dark pixels were chosen instead of only one for atmospheric correction in order to prevent taking the local atmospheric condition as the representative condition (Qi, et al., 2007; Chen, et al., 2011). To ensure that the atmospheric correction parameters hereinafter can reflect the regional situation, dark pixels should be selected as uniformly as possible according to the regional distribution of the dark areas (water leaving reflectance greater than zero in the 412 nm band) as shown in Fig.3. In this paper, 30 dark pixels were selected, and the corresponding coordinates and reflectance in the MERIS Level 1p data were obtained for the subsequent calculation.

3.2.2 *Selection of atmospheric correction bands*

Because of the oxygen or water vapor absorption, both the 761 nm and the 900 nm bands are characterized by very low atmospheric transmittances ($t(\lambda)$), i.e., $t(\lambda)$ is approximately 13% under standard middle-latitude summer atmosphere conditions (Liang, 2004); further, the MERIS Level 1p data in this study show that the reflectance of the relatively clean water is between 0.01 to 0.03, which is far less than the reflectance in the visible bands. Since the values of $t(\lambda)$ and $\rho_w(\lambda)$ are both numerically small, the value of $t(\lambda)$ and $\rho_w(\lambda)$ in Eq.(6) is close to zero. Accordingly, the TOA signal is almost entirely generated by the contribution of Rayleigh scattering and aerosol scattering, which is the theoretical basis of choosing these two bands for the calculation of the atmospheric correction parameter $\varepsilon(\lambda_i,\lambda_{NIR})$.

3.2.3 *Calculation of atmospheric correction parameter* $\varepsilon(\lambda_i,\lambda_{NIR})$

In Section 2.1, Eq.(10) and Eq.(11) provide two ways to interpolate the aerosol scattering reflectance from NIR to visible wavelength. To verify the suitability, behavior, and robustness, the two equations were tested under different aerosol models. This process was carried out by a simulation experiment using the software Second Simulation of the Satellite Signal in the Solar Spectrum (6S).

6S is one of the most comparatively perfect models in the world. It conducts atmospheric correction by simulating the transmission of solar radiation in the atmosphere (Vermote, et al., 1997a). In this study, five aerosol models, namely the biomass model, continental model, urban model, maritime model, and stratospheric model (Vermote, et al., 1997b), are examined Fig.4 shows an example of the parameter $\varepsilon(\lambda_i, 900)$ as a function of wavelength λ_i at a solar zenith angle of 60°, a sensor zenith angle of 45°, a relative azimuth angle of 90°, and a visibility of 22 km for these five aerosol models. In order to compare the two methods of visually calculating the atmospheric correction parameter $\varepsilon(\lambda_i, 900)$, we plot the data by logarithmic loordinates as shown in Fig.4.

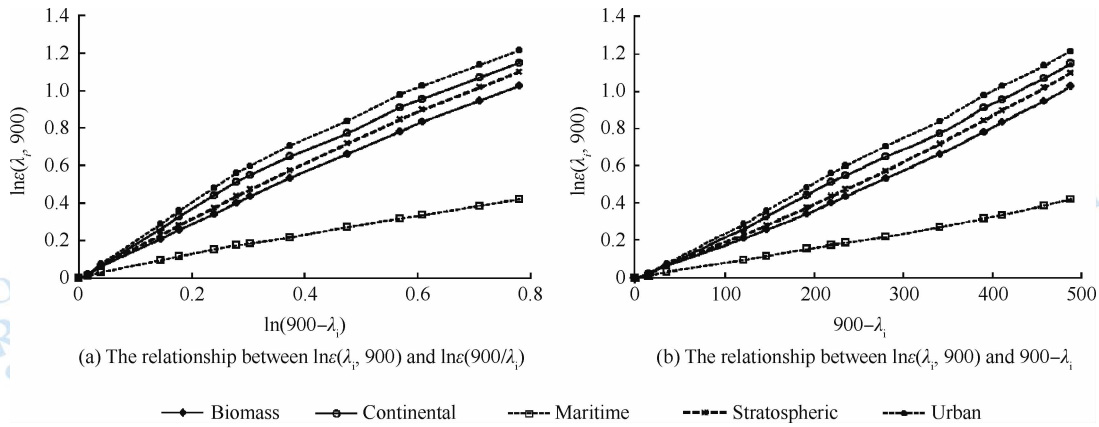

(a) The relationship between $\ln\varepsilon(\lambda_i, 900)$ and $\ln\varepsilon(900/\lambda_i)$ (b) The relationship between $\ln\varepsilon(\lambda_i, 900)$ and $900-\lambda_i$

Fig.4 Atmospheric correction parameter $\varepsilon(\lambda_i,900)$ as a function of λ_i for five aerosol models in logarithmic coordinates

As shown in Fig.4, the slopes of the lines are n (Fig.4(a)) and C (Fig.4(b)) in Eq.(10) and Eq.(11) respectively, which remain almost constant for a certain aerosol model. Fig.4(a) depicts that the linear relationship between $\ln(\varepsilon(\lambda_i,900))$ and $\ln(900/\lambda_i)$ is obvious for the urban model; however, the slopes of the other models decrease with an increase in $\ln(900/\lambda_i)$. In contrast, the linear relationship is more obvious in Fig.4(b) than in Fig.4(a).

A quantitative comparison of the performances of Eq.(10) and Eq.(11) with the same geometry and illumination conditions is given in Table 1 in order to compare the linear fitting accuracy of the two methods.

Table 1 Fitting accuracy of the two methods under the five aerosol models

Aerosol models	$\ln(\varepsilon(\lambda_i,\lambda_j)) = n\ln\left(\frac{\lambda_j}{\lambda_i}\right)$		$\ln(\varepsilon(\lambda_i,\lambda_j)) = C(\lambda_j-\lambda_i)$	
	Slope n	R^2	Slope C	R^2
Biomass	1.5858	0.9856	0.0025	0.9995
Continental	1.4942	0.9894	0.0024	0.9995
Maritime	1.4296	0.9976	0.0023	0.9961
Stratospheric	1.3321	0.9981	0.0021	0.9953
Urban	0.5338	0.9961	0.0008	0.9967

It is obvious that the aerosol wavelength dependence still holds true and that both equations can fit the wavelength dependence of $\varepsilon(\lambda_i, 900)$ very well (Table 1), with the coefficient of determination (R^2) larger than 0.985. Eq.(11) presents a higher determination coefficient than that in Eq.(10) as a whole, with the R^2 value of more than 0.995, performing more stably in the cases of all the five aerosol models. In comparison, Eq.(10) has poor stability for the continental model and the biomass model, with the determination coefficient (R^2) of less than 0.99. This is consistent with the findings of Wang & Gordon (1994) that the linear slip between $\ln(\varepsilon(\lambda_i,900))$ and $(900-\lambda_i)$ is relatively obvious. Accordingly, the atmospheric correction parameter ε is hereinafter calculated using Eq.(12) as Eq.(12),

$$\varepsilon(\lambda_i,\lambda_{NIR}) = \frac{\rho_A(\lambda_i)}{\rho_A(\lambda_{NIR})} = \exp(C(\lambda_{NIR}-\lambda_i)) \quad (12)$$

where ρ_A is the aerosol multiple-scattering reflectance. Thereafter, the aerosol scattering reflectance can be derived according to Eq.(12) as soon as we calculate the atmospheric correction parameter $\varepsilon(\lambda_i, \lambda_{900})$. Finally, the water-leaving reflectance of each band can be derived from Eq.(5) and Eq.(6).

4 RESULTS AND DISCUSSION

The performance of the atmospheric correction algorithm based on the black pixel assumption in the oxygen and the water-vapor absorption bands was evaluated by comparisons with *in situ* measurements and other atmospheric correction algorithms.

In this study, three popular indices, namely the Root Mean Square of Percentage (RMSP), the Relative Error (RE), and the Root Mean Square Error (RMSE), were used for assessing the accuracy of atmospheric correction, in which the definition expression of RMSE and RE was not repeated (Huang, 2011). RMSP is defined as Eq.(13),

$$\mathrm{RMSP} = \frac{\sqrt{\sum_{i=1}^{n}\left(\frac{V_{\mathrm{estimated}-i} - V_{\mathrm{measured}-i}}{V_{\mathrm{measured}-i}}\right)^2}}{n} 100\% \quad (13)$$

where $V_{\mathrm{estimated}-i}$ and $V_{\mathrm{measured}-i}$ are the measured and estimated values for the i^{th} sample site and n is the number of samples.

4.1 Comparison with *in situ* measurements

Using the abovementioned method, we corrected the MERIS images taken on Nov.11, 2007, Nov. 20, 2008, and April 25, 2009. Further, the estimated and the *in situ* measured values were compared using the two quasi-synchronous samples of each image (Fig.5).

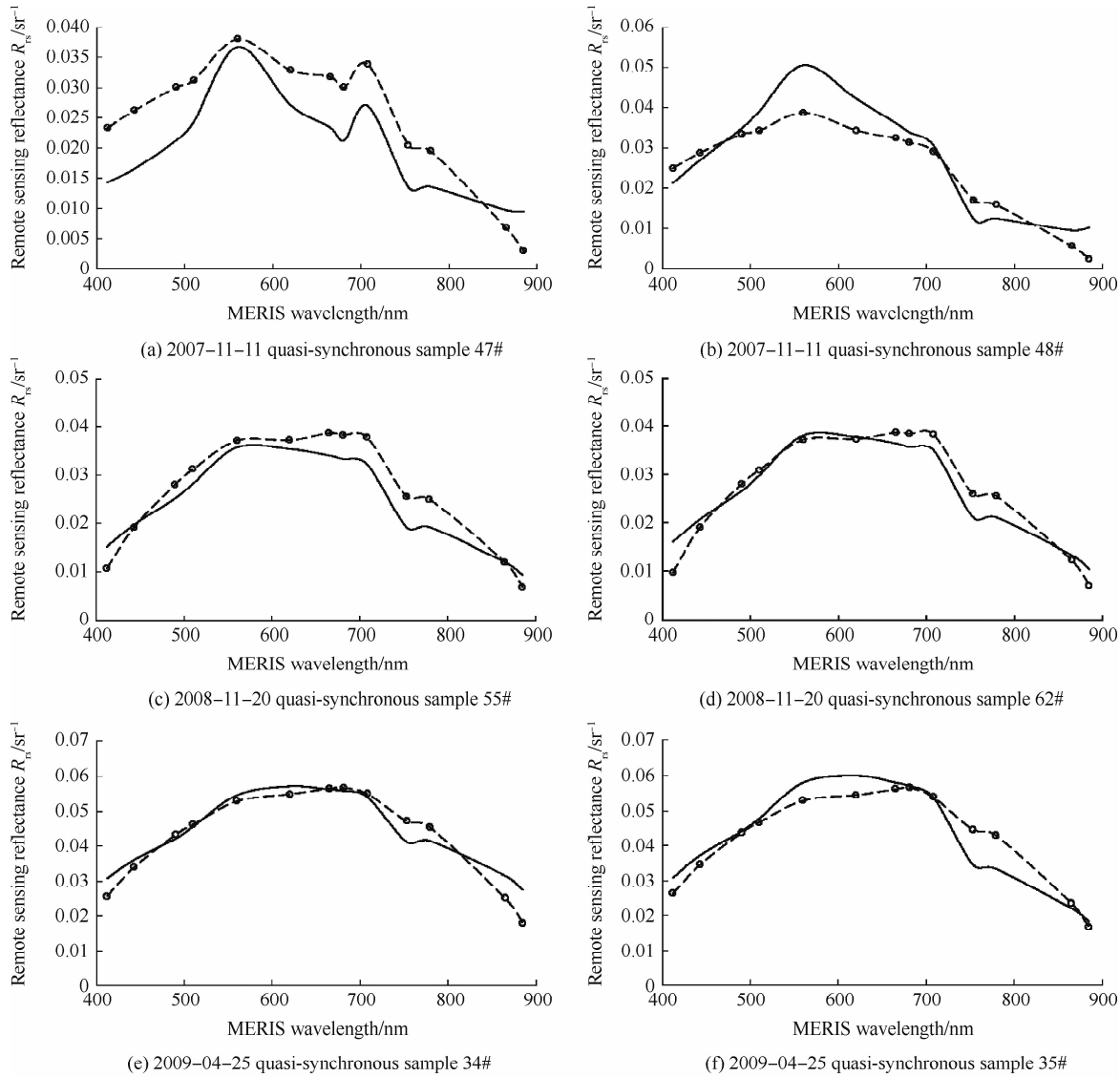

Fig.5 Comparisons between *in situ* measurements and MERIS-derived R_{rs} for two quasi-synchronous samples for the years 2007, 2008, and 2009

As shown in Fig.5, for the two quasi-synchronous samples, the spectrum of the derived values is consistent with the *in situ* measurements taken in 2007. The reflection peaks caused by the weak absorption of chlorophyll-a and carotene at 560 nm and the Raman scattering effect with algae water at 708 nm are all reflected in the spectrum, as well as the valley value caused by the strong absorption of chlorophyll-a in the red band of 681 nm, which, on the other hand, indicates that the overall spectral information is well preserved.

The other four quasi-synchronous samples for the years

2008 and 2009 are located in the central and the west regions of Taihu lake, respectively. As we know from Fig.1, Taihu lake is a typical shallow lake having an average depth of only 1.9 m. For the same wind speed, the tangential stress in the central region will be stronger than in the bay region and off the shore because of the open water surface and the relatively long blowing process. Moreover, the wind speed is greater by 0.5—1 m/s in the central region than off the shore; this leads to a relatively high concentration of suspended matter (Sun, et al., 1993; Zhang, et al., 2006). The surface runoff carried a large amount of suspended particles, and the open water was susceptible to the influence of wind and waves; all these contributes to the high suspended matter concentration in the west region of Taihu lake (Sun, et al., 2008), which in turn concealed the absorption valley and the fluorescence peak of the pigment particles at 675 nm and 708 nm. The spectra of the measured and the derived water leaving reflectance for the years 2008 and 2009 all match well, which demonstrates that the algorithm proposed in this paper has some applicability in both turbid waters and algae-containing waters.

To quantitatively assess the accuracy of the proposed algorithm, we calculated the ARE, RMSP, and RMSE between the measured and the estimated reflectance of the MERIS bands (Table 2). For the five considered sites, on Nov.11, 2007, the Average Relative Error (ARE) was less than 0.45 except for band 14 (885 nm) with ARE of up to 0.7231; band 6 (620 nm) had the highest correction accuracy with ARE of 0.0134. For the six considered sites, on November 20, 2008, ARE was less than 0.4 except for band 1 (412 nm) and band 14 (885 nm), with RMSP of less than 20%. For the six considered sites, on April 25, 2009, ARE was less than 0.4 except for band 10 (754 nm) with RMSP of less than 25%.

In general, MERIS band 3—band 9 have relatively high correction accuracy as compared to the blue and the infrared bands. It is possible that the turbid inland waters containing chlorophyll and a yellow substance has a strong absorption effect in the blue bands, leading to the low water-leaving reflectance. Further, the water signal is a very small proportion of the total signal because of the strong Rayleigh scattering and aerosol scattering; hence, a small correction deviation can cause a large relative error (Xu, et al., 2011). Moreover, for the relatively large ARE in the NIR bands, this is probably because of the fact that the overall signal is relatively weak as compared to the other bands (Zhou, et al., 2011).

Table 2 Accuracy evaluation of atmospheric correction results for MERIS bands

MERIS band	Central wavelength/nm	2007-11-11			2008-11-20			2009-04-25		
		ARE	RMSP/%	RMSE	ARE	RMSP/%	RMSE	ARE	RMSP/%	RMSE
1	412	0.4011	27.53	0.0050	0.4116	16.42	0.0068	0.0088	10.94	0.0058
2	443	0.3257	26.26	0.0056	0.1613	8.60	0.0047	0.0908	10.66	0.0057
3	490	0.1870	17.23	0.0055	0.0269	5.81	0.0039	0.1333	10.44	0.0063
4	510	0.0799	11.72	0.0050	0.0424	5.57	0.0041	0.1042	9.07	0.0063
5	560	0.0997	4.69	0.0044	0.1263	6.93	0.0064	0.0271	6.57	0.0065
6	620	0.0134	9.26	0.0051	0.0725	4.97	0.0047	0.0404	7.50	0.0076
7	665	0.1276	15.80	0.0059	0.0228	4.40	0.0048	0.1146	9.71	0.0083
8	681	0.1696	18.66	0.0060	0.0509	4.82	0.0050	0.1355	10.40	0.0085
9	708	0.1040	14.88	0.0063	0.0002	6.15	0.0077	0.1208	9.61	0.0079
10	754	0.4473	40.90	0.0052	0.1659	11.64	0.0074	0.4199	22.81	0.0096
12	779	0.3527	36.19	0.0048	0.1441	11.00	0.0074	0.3623	20.55	0.0092
13	865	0.3545	13.54	0.0016	0.0886	10.12	0.0064	0.1066	16.69	0.0089
14	885	0.7231	27.05	0.0031	0.3245	14.64	0.0068	0.0426	15.87	0.0098
Mean	—	0.2604	20.29	0.0049	0.1260	8.54	0.0059	0.1313	12.37	0.0077

4.2 Comparison with other atmospheric correction algorithms

To access the performance of the proposed algorithm, we compared the atmospheric correction results with 6S, an improved dark pixel algorithm proposed by Huang (2011), and the Beam C2R algorithm.

Among them, the 6S processor required synchronization meteorological data to provide a relatively accurate correction result. In this study, we derived the aerosol thickness from the collected AERONET data of Taihu lake for three dates, i.e., 0.553, 0.3429, and 1.031, respectively, taken as the input parameters of the 6S processor. This led to better results than those obtained using the default visibility of 15 km (aerosol thickness: 0.315) as the input parameter. The modified dark pixel algorithm was carried out by Huang, et al. (2011); it consists of three steps: first, the selection of some dark pixels in the MERIS Level 2p data and extraction of the water leaving reflectance; second, the calculation of the path radiation reflectance by removing the water leaving reflectance provided by the MERIS Level 2p data from the TOA reflectance provided by the MERIS Level 1p data; and finally, the atmospheric correction for the entire area by the elimination of the average path radiation reflectance (Huang, 2011). The Beam C2R algorithm, as mentioned above, is a case II atmospheric correction algorithm embedded in the Beam 4.8 processor on the basis of the neural network model (Roland, et al., 2008). The correction result of all the four algorithms and the *in situ* measurements are depicted in Fig.6.

As shown in Fig.6, the spectra of the two quasi-synchronization samples match very well with the *in situ* measurements for the year 2007, and so do those in the case of the 6S processor for the years 2007 and 2008. However, 6S performs poorly for the year 2009 with a large overestimation, which is probably caused by the light cloud on April 25, 2009. The modified dark pixel algorithm performs well for the year 2007 with a small underes-

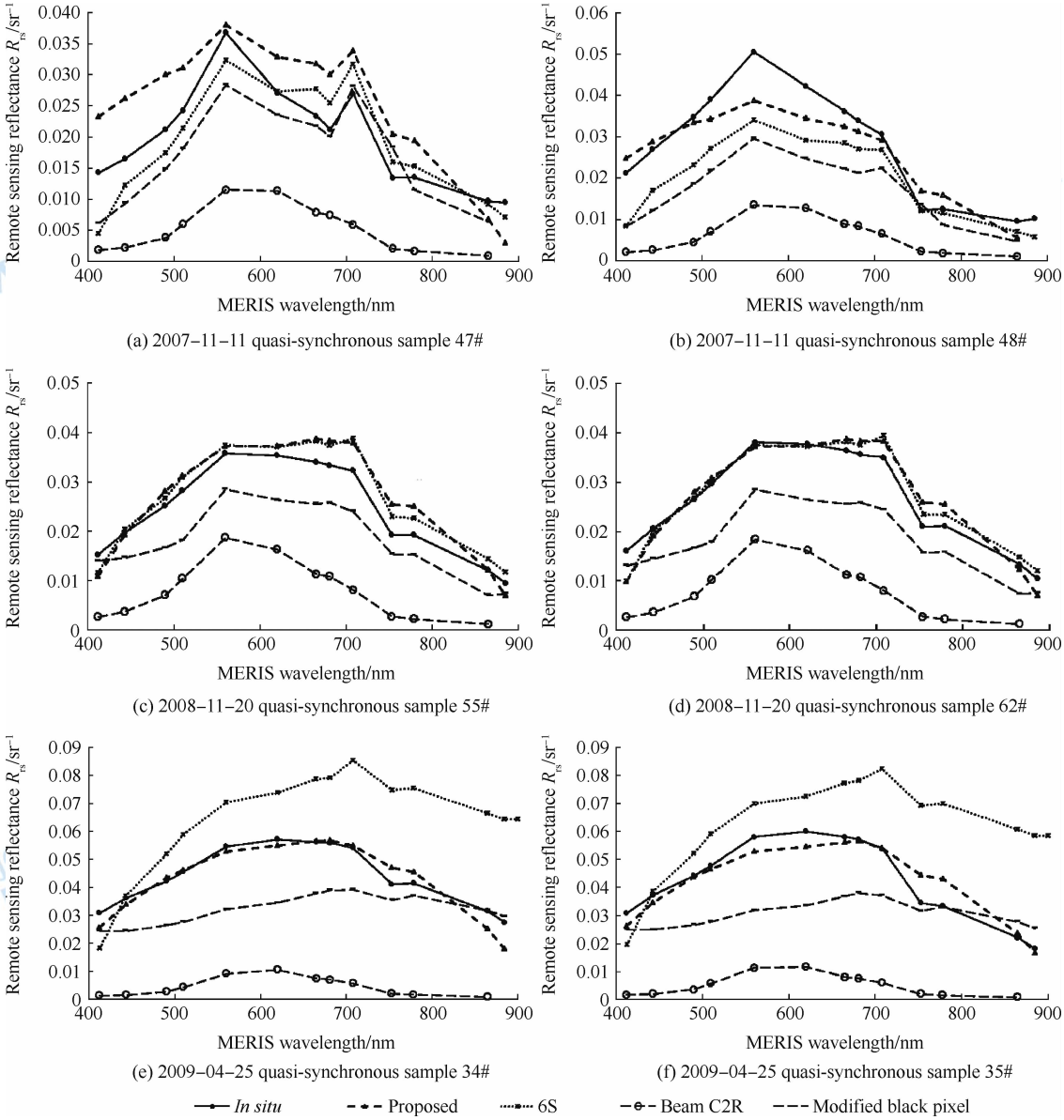

Fig.6 Comparisons between derived water leaving reflectance of four algorithms and *in situ* measurements

timation; however, for the years 2008 and 2009, the derived results have a relatively large degree of underestimation as compared to that for the year 2007. Beam C2R performed poorly; this could be attributed to the fact that the atmospheric parameters in the method were predetermined by the NN method, with the training data mostly collected from European lakes whose water constituents and bio-optical features were considerably different from those of Asian waters (Roland, et al., 2008), such as our study area, Taihu lake.

For a quantitative assessment of the accuracy of the proposed algorithm, Table 3 presents the average evaluation indices of the MERIS 13 bands for the four different atmospheric correction algorithms, among which ARE is the average value of the absolute relative error.

It can be observed that the ARE value of the proposed algorithm for the years 2007 and 2008 is 0.2604 and 0.126, respectively, larger than that of 6S (Table 3). The better performance of 6S is probably because of the synchronous measured aerosol thickness from AERONET. In contrast, the ARE of our atmospheric correction method for the year 2009 is as low as 0.1313,

Table 3 Accuracy of four algorithms

Method	2007-11-11			2008-11-20			2009-04-25		
	ARE	RMSP/%	RMSE	ARE	RMSP/%	RMSE	ARE	RMSP/%	RMSE
Proposed method	0.2604	20.2863	0.0049	0.1260	8.5442	0.0059	0.1313	12.3701	0.0077
6S	0.1880	15.8923	0.0052	0.0729	7.7334	0.0060	0.5569	31.4296	0.0111
Modified black pixel	0.2808	15.7284	0.0053	0.3703	14.7905	0.0081	0.3944	21.7756	0.0124
Beam C2R	0.7945	31.3332	0.0089	0.7573	28.6722	0.0122	0.8968	44.8558	0.0204

two times less than that of 6S and the other methods. The RMSP values of the three days of 2007, 2008, and 2009 are 20.29%, 8.54%, and 12.37%, respectively, with an average accuracy of up to 80%. It should be noted that the ARE and RMSP values of November 11, 2007, are both larger than those of November 20, 2008, and April 25, 2009, which indicates that the proposed algorithm performs better in turbid waters than in the waters dominated by plankton. However, the proposed algorithm also has accuracy of up to approximately 80%. The numerical order of RMSE for the years 2007, 2008, and 2009 is as proposed algorithm < aerosol-thickness-assisted 6S < modified black pixel algorithm < Beam C2R. In the case of the proposed algorithm, the RMSE values for the years 2007, 2008, and 2009 are 0.0049, 0.0059, and 0.0077, respectively, which indicates that the proposed algorithm has a stable performance for all the considered samples for certain days.

5 CONCLUSIONS

(1) In this study, two specific NIR bands provided by the MERIS data, i.e., the oxygen and water-vapor absorption bands were introduced to improve the atmospheric correction method for inland turbid waters. The two bands maintained the validity of the assumption that the water leaving reflectance approached zero. The spectra of the corrected quasi-synchronization samples matched very well with the *in situ* measurements, particularly in band 3 to band 9 (from 490 nm to 708 nm).

(2) By comparing the performance of 6S, modified black pixel algorithm, Beam C2R, and the proposed algorithm, we learnt that the aerosol-thickness-assisted 6S exhibited better performance on a cloudless fine weather day. However, the scarcity of the synchronization aerosol data limited the application of this method. The modified black pixel algorithm could be simply operated and provided guaranteed accuracy but was difficult to improve further. Beam C2R exhibited the worst performance with a significant underestimation among the four algorithms. In summary, the proposed algorithm performed well with acceptable accuracy of up to approximately 80% according to the data of the three quasi-synchronous experiments; it also had stable performance and certain applicability.

(3) The value of $\varepsilon(\lambda_i, \lambda_{NIR})$ in the proposed algorithm was the mean value of that of the selected multiple black pixels; it was considered to be the atmospheric correction parameter of the entire area. Although this data processing reduced the error of using only a single dark pixel, it smoothed the regional aerosol differences of the lake. Therefore, we will attempt to improve the accuracy of the proposed algorithm by using an aerosol partition in the future.

REFERENCES

Ångström A. 1964. The parameters of atmospheric turbidity. Tellus, 16 (1): 64-75 [DOI: 10.1111/j.2153-3490.1964.tb00144.x]

Bourg L, D'Alba L and Colagrande P. 2008. Meris smile effect characterization and correction [J/OL]. http://earth.eo.esa.int/pcs/envisat/meris/documentation/MERIS_Smile_Effect.pdf

Chen J, Sun J H and Fu J. 2011. Using the sub-area dark pixel and spline interpolation approach to estimate the aerosol optical thickness on Taihu Lake. Remote Sensing Information, (3): 33-37

Chen Y Z, Wang X Q and Gao Z L. 2008. Atmospheric correction of MERIS data over the Taiwan Straits. Marine Sciences, 32(3): 62-67

Doerffer R and Schiller H. 2008. MERIS Regional Coastal and Lake Case 2 Water Project Atmospheric Correction ATBD. Version 1.0

Gordon H R, Brown J W and Evans R H. 1988. Exact Rayleigh scattering calculations for use with the Nimbus-7 Coastal Zone Color Scanner. Applied Optics, 27(5): 862-871 [DOI: 10.1364/AO.27.000862]

Gordon H R and Wang M H. 1994a. Retrieval of water-leaving radiance and aerosol optical thickness over the oceans with SeaWiFS: a preliminary algorithm. Applied Optics, 33(3): 443-452 [http://www.ncbi.nlm.nih.gov/pubmed/20862036]

Gordon H R and Wang M H. 1994b. Influence of oceanic whitecaps on atmospheric correction of ocean-color sensors. Applied Optics, 33 (33): 7754-7763 [http://www.ncbi.nlm.nih.gov/pubmed/20962986]

Gould R W Jr, Arnone R A and Martinolich P M. 1999. Spectral dependence of the scattering coefficient in case 1 and case 2 waters. Applied Optics, 38 (12): 2377-2383 [DOI: 10.1364/AO.38.002377]

He X Q, Pan D L, Bai Y, Zhu Q K and Gong F. 2007. Vector radiative transfer numerical model of coupled ocean-atmosphere system using matrix-operator method. Science in China Series D: Earth Sciences, 50(3): 442-452 [DOI: 10.1007/s11430-007-2075-4]

Hu C M, Carder K L and Muller-Karger F E. 2007. Atmospheric correction of SeaWiFS imagery over turbid coastal waters: a practical method. Remote Sensing of Environment, 74(2): 195-206 [DOI: 10.1016/S0034-4257(00)00080-8]

Huot J P, Tait H, Rast M, Delwart S, Bézy J L and Levrin G. 2001. The optical imaging instruments and their applications: AATSR and MERIS. ESA Bulletin, 106: 56-66

Huang C H. 2011. Retrieval of Water Constituents by Bio-optical Algorithm Considering the Vertical Distribution of Suspended Particle in Taihu Lake. Nanjing: Nanjing Normal University, 79-80

Kuchinke C P, Gordon H R and Franz B A. 2009. Spectral optimization for constituent retrieval in case 2 waters I: implementation and performance. Remote Sensing of Environment, 113(3): 571-587 [DOI: 10.1016/j.rse.2008.11.001]

Le C F, Li Y M, Zha Y, Sun D Y and Wang L Z. 2008. Inversion of hyperspectral reflectance for estimating suspended matter concentration in Lake Taihu. Acta Scientiae Circumstantiae, 28(10): 2148-2155

Li S J and Wang X J. 2003. Relationship between suspended matter concentration and spectral reflectance of Chao Lake. Urban Environment and Urban Ecology, 16(6): 66-68

Li Y M, Wang Q, Huang J Z, Lv H and Wei Y C. 2006. Inversing chlorophyll concentration of Taihu Lake by analytic model. Journal of Remote Sensing, 10(2): 169-175

Li Y M, Wang Q, Huang J Z, Lv H and Wei Y C. 2010. The Optical Characteristics of Taihu Lake and Water Color Remote Sensing. Beijing: Science Press: 2-3

Liang S L. 2004. Quantitative Remote Sensing of Land Surfaces. New York: Wiley-Interscience: 46-51

Lu C P, Lv H and Li Y M. 2012. Backscattering properties and parametric model of Taihu Lakebased on spectral classification. Journal of Remote Sensing, 16(2): 419-436

Moore G F, Aiken J and Lavender S J. 1999. The atmospheric correction of water colour and the quantitative retrieval of suspended particulate matter in Case II waters: application to MERIS. International Journal of Remote Sensing, 20(9): 1713-1733 [DOI: 10.1080/014311699212434]

Qi Z X and Deng R R. 2007. The Atmospheric correction method for nonhomogeneous atmosphere based on many dark objects. Remote

Sensing for Land and Resources, 72(2): 16-19

Ruddick K G, Ovidio F and Rijkeboer M. 2000. Atmospheric correction of SeaWiFS imagery for turbid coastal and inland waters. Applied Optics, 39(6): 897-912 [DOI: 10.1364/AO.39.000897]

Siegel D A, Wang M H, Maritorena S and Robinson W. 2000. Atmospheric correction of satellite ocean color imagery: the black pixel assumption. Applied Optics, 39(21): 3582-3591 [DOI: 10.1364/AO.39.003582]

Sun D Y, Li Y M, Wang Q, Le C F, Huang C C and Wu L. 2008. The scattering characteristics of Lake Taihu waters. Journal of Lake Sciences, 20(3): 389-395

Sun S C and Huang Y P. 1993. Taihu Lake. Beijing: Maritime Press: 10-11

Tang J W, Tian G L, Wang X Y, Wang X M and Song Q J. 2004. The methods of water spectra measurement and analysis Ⅰ: above-water method. Journal of Remote Sensing, 8(1): 37-44

Vermote E F, Tanré D, Deuzé J L, Herman M and Morcrette J J. 1997a. Second Simulation of the Satellite Signal in the Solar Spectrum, 6S: An Overview. IEEE Transactions on Geoscience and Remote Sensing, 35(3): 675-686 [DOI: 10.1109/36.581987]

Vermote E F, Tanré D, Deuzé J L, Herman M and Morcrette J J. 1997b. Second Simulation of the Satellite Signal in the Solar Spectrum (6S). 6S User Guide Version 2

Wang M H and Gordon H R. 1994. A simple, moderately accurate, atmospheric correction algorithm for SeaWiFS. Remote Sensing of Environment, 50(3): 231-239 [DOI: 10.1016/0034-4257(94)90073-6]

Wang M H. 2007. Remote sensing of the ocean contributions from ultraviolet to near-infrared using the shortwave infrared bands: simulations. Applied Optics, 46(9): 1535-1547 [DOI: 10.1364/AO.46.001535]

Xu H, Gu X F, Li Z Q, Li L and Chen X F. 2011. Atmospheric correction method for HJ-1 CCD imagery over waters based on radiative transfer model. Spectroscopy and Spectral Analysis, 31(10): 2798-2803

Yang J H, Wang J and Zhao D ZH. 2008. Review on the atmospheric correction of ocean color remote sensing. Marine Environmental Science, 27(1): 97-100

Zhang M W, Tang J W and Ding J. 2008. Summarization of ocean color atmospheric correction algorithm. Ocean Technology, 27(3): 110-114

Zhang Y L, Feng S, Ma R H, Liu M L and Qing B Q. 2008. Spatial pattern of euphotic depth and estimation of phytoplankton primary production in Lake Taihu in autumn. Journal of Lake Sciences, 20(3): 380-388

Zhang Y L, Qing B Q, Hu W P, Wang S M, Chen Y W and Chen W M. 2006. Spatial variation of euphotic depth in Taihu Lake and its ecological significance. Science in China (Series D: Earth Sciences), 36(3): 287-296

Zhou L G, Ma W C, Gu W H and Huai H Y. 2011. Atmospheric correction of HJ-1 CCD data for water imagery based on dark object model. Spectroscopy and Spectral Analysis, 31(8): 2238-2242

Zhu J J, Chen J, Matsushita B, Yang W and Fukushima T. 2012. Atmospheric correction of ENVISAT/MERIS data over case II waters: the use of black pixel assumption in oxygen and water vapour absorption bands. International Journal of Remote Sensing, 33(12): 3713-3732 [DOI: 10.1080/01431161.2011.632656]

利用氧气和水汽吸收波段暗像元假设的MERIS影像二类水体大气校正方法

檀静[1]，李云梅[1]，赵运林[2]，吕恒[1]，徐德强[3]，周莉[1]，刘阁[1]

1.南京师范大学 虚拟地理环境教育部重点实验室，江苏 南京 210046;
2.湖南城市学院，湖南 益阳 413000;
3.宜兴市水文水资源监测中心，江苏 宜兴 214200

摘 要:MERIS数据以其更为合理的水色波段设置和300 m较高的空间分辨率,在内陆湖泊水环境遥感监测中有较大的应用潜力,对其进行有效的大气校正则是水环境参数定量化反演的前提。以太湖为研究区,研究基于氧气和水汽吸收波段的暗像元为假设条件,改进传统的近红外波段暗像元大气校正方法,采用MERIS level 2p数据辅助获取湖区气溶胶参数,并利用2007-11-11、2008-11-20以及2009-04-25等3景MERIS影像进行验证。结果表明,该方法能够快速、有效地完成MERIS影像的大气校正,与地面准同步实测数据相比,3次校正的均方根百分比RMSP(Root Mean Square of Percentage)、都在25%以下; 与Beam自带的二类水体大气校正算法、气溶胶厚度辅助的6S大气校正以及改进的暗像元算法进行精度比较,结果表明该方法校正精度较高。由于该方法不需要同步实测气溶胶数据,因此具有一定的适用性。

关键词:大气校正,MERIS,二类水体,吸收波段

中图分类号:TP751 **文献标志码**:A

引用格式:檀静,李云梅,赵运林,吕恒,徐德强,周莉,刘阁.2013.利用氧气和水汽吸收波段暗像元假设的MERIS影像二类水体大气校正方法.遥感学报,17(4):768-787

Tan J, Li Y M, Zhao Y L, Lv H, Xu D Q, Zhou L and Liu G. 2013. Atmospheric correction of MERIS data on the black pixel assumption in oxygen and water vapor absorption bands. Journal of Remote Sensing, 17(4): 768-787

[DOI: 10.11834/jrs.20132102]

1 引 言

在水色遥感中,传感器在大气层顶接收到的信号TOA(Top of Atmosphere)中90%以上来自大气散射,而水体信息在可见光范围内最多只占到10%(Huot等, 2001),大气散射信息对水体光谱信息造成了极大的干扰,严重影响了水环境参数的遥感提取。因此,要提高水环境遥感监测精度,必须考虑大气的影响。大气散射由大气分子散射(瑞利散射)以及气溶胶散射组成,由于大气分子成分及含量比较稳定,大气分子散射贡献已能通过多次散射加偏振的精确瑞利散射计算得到(Gordon 等, 1988; He等, 2007),而气溶胶在空间域及时间域上变化较大,要准确计算其散射比较困难,故不同大气校正算法的区别主要体现在如何计算气溶胶散射,以及大气分子与气溶胶的共同作用等方面。

传统的大气校正算法中气溶胶散射部分的计算多是建立在黑暗像元的假设条件上,即假设水体在近红外波段(NIR>700 nm)的离水辐亮度近似为0,近红外波段的信号值主要来自于瑞利散射以及气溶胶散射,且气溶胶随着波长的变化表现出一定的规律性(Gould 等, 1999),在此基础上NIR(Near Infraved)标准算法,将近红外波段的气溶胶散射外推到可见光波段范围内,从而得到各波段的离水辐亮度。对于一类水体,其光学特性主要由浮游植物及其伴生物决定,大洋开阔水体为典型的一类水体;

收稿日期:2012-03-28;**修订日期**:2012-10-05;**优先数字出版日期**:2012-10-13

基金项目:国家自然科学基金(编号: 40971215);环保公益性行业科研专项(编号:2010467022);江苏省高校自然科学研究重大项目(编号: 11KJA170003);江苏省2011年度普通高校研究生科研创新计划(编号: CXLX_0875)

第一作者简介:檀静(1987—),女,硕士研究生,现从事高分辨率遥感、遥感影像大气校正的理论和应用研究。E-mail: tanjing871015@163.com

通信作者简介:李云梅(1966—),女,教授,主要从事环境遥感方向的研究。E-mail: liyunmei@hjhu.edu.cn

而二类水体的光学特性则由悬浮泥沙及黄色物质决定，受陆源物质排放影响较严重的内陆及近岸水体多为二类水体(张民伟 等, 2008; 杨健洪 等, 2008)而言，由于浑浊水体在近红外波段的高反射使得近红外离水辐亮度近似为 0 的假设不再成立，因此该方法无法直接应用于二类水体(Siegel 等, 2000)。

Hu 等人(2000)在上述一类水体大气校正算法的基础上提出了针对二类水体的大气校正算法，该算法假设气溶胶类型在小范围内(约 50—100 km)不变。为此，首先在较清洁水体区域，应用清洁水体标准算法确定气溶胶类型，然后，将该类型按照最临近准则传递到混浊区域; Ruddick 等人(2000)在 NIR 标准算法的基础上，提出了两个假设:(1)765 nm 和 865 nm 波段气溶胶多次散射反射率之比在所研究区域不变; (2)经过大气漫射透过率 T_0(从太阳到海面) 校正的 765 nm 和 865 nm 波段海水反射率之比不变。进而联立方程求解 NIR 波段水体的离水反射率; Kuchinke 等人(2009)建立了二类水体光谱优化算法，再结合生物光学模型与气溶胶模型(用 Junge 谱描述)来计算气溶胶反射率; Wang(2007)提出了 NIR/SWIR(Near Infraved/Short Wave Infraved) 算法，即将 NIR 算法中近红外波段用 MODIS 的短波红外波段来代替，认为二类水体在短波红外波段的强吸收造成其在这些波段的离水辐亮度极小，可以忽略不计，使得该算法的准确性提高，得到了较好的校正效果。

针对 MERIS 数据，由于缺少短波红外波段，SWIR(Short Wave Infraveel)算法不能适用，因此发展了一种针对二类水体的神经网络算法 C2R (MERIS Regional Case 2 Water Algorithms) (Doerffer 和 Schiller, 2008)，并嵌入在 Beam 4.8 软件中；另外，黄昌春(2011)也针对 MERIS 数据提出了一个修正的算法，即利用 MERIS Level 2p 产品中大气校正成功样点的遥感反射率对 MERIS Level 1p 产品的大气程辐射进行修正，误差在可接受范围内。

Zhu 等人(2012)用 MERIS 数据的两个特殊波段(761 nm 氧气吸收波段和 900 nm 水汽吸收波段)代替传统的近红外波段来选取二类水体暗像元，确定研究区大气气溶胶性质，从而对研究区域进行大气校正，得到了较好的校正效果。本文在此算法的基础上，利用 MERIS Level 2p 产品辅助选取暗像元，从而对该算法进行了改进。同时，还将本文方法与 Beam 自带的二类水体算法(以下简称 Beam C2R 算法)、基于气溶胶厚度的 6S 大气校正算法以及黄昌春提出的改进的暗像元算法进行精度比较。

2 研究区与数据

2.1 研究区概况

太湖是中国 5 大淡水湖之一，湖泊面积 2427.8 km^2，湖中岛屿 51 个，实际水面面积为 2338.1 km^2，湖岸线总长 405 km，湖泊平均水深 1.9 m，属于典型的大型浅水内陆湖泊(孙顺才和黄漪平，1993; 李云梅 等，2010)。太湖界于 30° 55′ 40″—31° 32′ 58″ N、119°52′32″— 120°36′10″E，位于长三角地区内陆发达城市之间，水质状况受陆源排放以及人类活动影响显著，水体光学特性由叶绿素、悬浮物以及黄色物质等共同决定，复杂多变，是典型的二类水体(张运林 等, 2008)。

2.2 数据及处理

2.2.1 影像数据及其预处理

分别获取了 2007-11-11、2008-11-20 及 2009-04-25 等 3 幅 MERIS 300 m 分辨率的 MERIS Level 1p 和 MERIS Level 2p 影像数据。MERIS 是欧洲太空局于 2002-03-01 发射的环境遥感卫星(ENVISAT) 上搭载的一种传感器，主要用于海洋和海岸带的水色监测(陈芸芝 等, 2008)。MERIS Level 1p 数据是对传感器获得的 DN 值(Digital Number)进行定标处理后大气层顶反射率数据，MERIS Level 2p 数据是对 MERIS Level 1p 数据进行大气校正后得到的数据。与 SeaWiFS 和 MODIS 数据相比，MERIS 波段设置较窄，用于常规大气校正的两个波段为第 12 波段(中心波长 778. 75 nm，带宽 15 nm)和第 14 波段(中心波长 885 nm，带宽 10 nm); 此外，MERIS 数据还设置了专门的氧气和水汽吸收波段，中心波长分别为 760.16 nm(带宽 3.75 nm)、900 nm (带宽 10 nm)。

数据预处理在 Beam 4.8 中进行，为了去除影像中数据重叠现象，对获取的 MERIS Level 1P 影像进行微笑效应纠正(Smile Correction Processor)(Bourg, 2008)。由于影像数据中给出的是辐亮度值，而在下面要进行的大气校正过程中，无量纲的反射率 ρ 更加便于运算，故而对影像进行辐亮度到反射率的转化(Gordon 和 Wang, 1994a):

$$\rho = \pi L / F_0 \cos\theta_0 \qquad (1)$$

式中，ρ 为大气层外反射率，L 为大气层外辐亮度，

F_0 为大气层外辐照度,θ_0 为太阳天顶角。

2.2.2 地面同步实验数据

分别于2007-11-11、2008-11-20以及2009-04-25共进行了3次地面实验,获取了样点的水面遥感反射率数据,3次采样样点分布、编号以及太湖水深分布如图1所示。

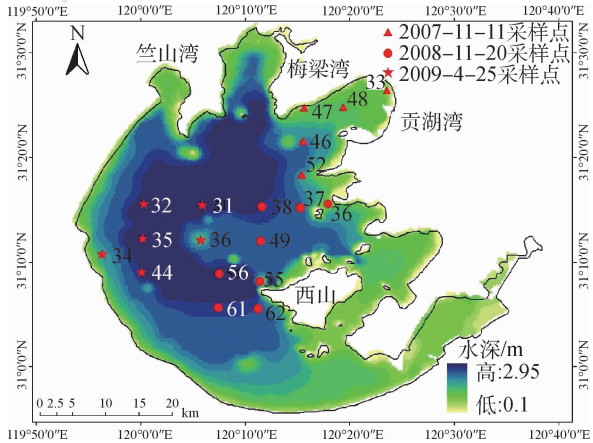

图1 太湖样点及水深分布图

水面的反射光谱采用美国ASD公司生产的ASD FieldSpec Pro便携式光谱辐射计测量,其波段范围为350—1050 nm,光谱分辨率为2 nm。为减少水体镜面反射和船体阴影的影响,更好地提取出反映水体信息的离水辐亮度和遥感反射率 R_{rs},测量时采用唐军武等(2004)提出的关于内陆二类水体水面以上光谱测量的方法。测量时,天空晴朗无云,湖面平静,待船停稳后,在甲板开阔处(距水面1 m左右)分别测量标准灰板、遮挡标准灰板、水体和天空光的光谱信息,以上4个参数各测量10条光谱曲线,在测量水面反射光谱的同时记录各测点的GPS坐标和当时的风速、风向以及时间。遥感反射率利用式(2)进行提取:

$$R_{rs}=\frac{(L_{sw}-rL_{sky})\cdot\rho_p}{L_p\pi} \tag{2}$$

式中,R_{rs} 为遥感反射率,L_{sw} 为总的辐亮度,L_{sky} 为天空漫散射光,不带有任何水体信息,r 参照唐军武等(2004)的研究取值为0.025,L_p 为标准灰板实测值,ρ_p 为参考板的反射率。

3 基于氧气和水汽吸收波段暗像元假设的大气校正方法

3.1 传统的NIR/SWIR算法

在水体-大气系统条件下,卫星遥感器接收到的总信号 $\rho_t(\lambda)$ 为:

$$\rho_t(\lambda)=\rho_r(\lambda)+\rho_a(\lambda)+T\rho_g(\lambda)+t\rho_{wc}(\lambda)+t\rho_w(\lambda)+t\rho_b(\lambda) \tag{3}$$

式中,$\rho_r(\lambda)$ 为大气分子瑞利散射,$\rho_a(\lambda)$ 为气溶胶散射,$\rho_g(\lambda)$ 为太阳耀斑辐射,$\rho_{wc}(\lambda)$ 为白帽辐射,$\rho_w(\lambda)$ 为离水反射率,$\rho_b(\lambda)$ 为来自水底的反射辐射,t 为大气漫射透过率,T 为大气直射透过率。

当数据中没有突变值时,可以忽略太阳耀斑的影响。此外,对于较浑浊的二类水体而言,来自底部的反射辐射难以透射到水表,可以忽略不计。白帽反射率在风速低于4 m/s时为0,而当风速在4—7 m/s时,其值的数量级为 10^{-4},远小于反射率的数量级 10^{-2},故白帽反射率也可忽略不计(Gordon和Wang, 1994b)。因此,当不考虑太阳耀斑、白帽反射以及底质影响时,卫星接收到的大气层外总反射率为:

$$\rho_t(\lambda)=\rho_r(\lambda)+\rho_a(\lambda)+t\rho_w(\lambda) \tag{4}$$

大气漫射透射率 t 主要受大气分子散射、臭氧吸收等因素的影响,可按式(5)计算(Siegel等, 2000):

$$t=\exp(-(\tau_r/2+\tau_{OZ})/\cos\theta) \tag{5}$$

式中,τ_r 为大气分子瑞利散射光学厚度;τ_{OZ} 为臭氧光学厚度;θ 为卫星天顶角。

本文中瑞利散射通过成熟的算法计算(He, 2007),去除瑞利散射后的反射率 $\rho_c(\lambda)$ 只与气溶胶反射以及离水反射率有关:

$$\rho_c(\lambda)=\rho_a(\lambda)+t\rho_w(\lambda) \tag{6}$$

在只考虑气溶胶单次散射的情况下:

$$\rho_a(\lambda)=\rho_{as}(\lambda)=\omega_a(\lambda)\tau_a(\lambda)p_a(\theta,\theta_0,\lambda)/4\cos\theta\cos\theta_0 \tag{7}$$

式中,$\rho_{as}(\lambda)$ 为单次散射反射率,ω_a、τ_a 分别为气溶胶单次散射反照率和气溶胶厚度,p_a 为气溶胶单次散射相函数,与观测几何以及波长有关。

两个波长处的单次散射反射率具有比例关系,即可以定义一个大气校正参数 $\varepsilon(\lambda_i,\lambda_j)$ 进行计算(Wang和Gordon, 1994),其表达式如下:

$$\varepsilon(\lambda_i,\lambda_j)=\frac{\rho_{as}(\lambda_i)}{\rho_{as}(\lambda_j)}=\frac{\omega_a(\lambda_i)\tau_a(\lambda_i)P_a(\theta,\theta_0,\lambda_i)}{\omega_a(\lambda_j)\tau_a(\lambda_j)P_a(\theta,\theta_0,\lambda_j)} \tag{8}$$

式中,λ_i 为短波波长,λ_j 为长波波长,一般选择离水反射率为0的波段计算 $\varepsilon(\lambda_i,\lambda_j)$。对于同一种气溶胶模型来说,$\omega_a$ 可以认为是定值,而单次散射相函数 P_a 是观测几何与波长 λ 的函数。大量实测数据的统计研究发现,单次散射相函数之比也可以看作常数,而在Junge谱下,气溶胶厚度是关于波长的负指数函数(Ångström,1964):

$$\tau_a(\lambda)=\sigma\lambda^{-\beta} \quad (9)$$

式中，σ 为大气浑浊指数，β 为埃斯特朗系数，在一定的气溶胶模型下其值为常数，从而式(8)可以简化为两个波长处气溶胶厚度之比，得到如下表达式：

$$\varepsilon(\lambda_i,\lambda_j)=\frac{\rho_{as}(\lambda_i)}{\rho_{as}(\lambda_j)}=\frac{\tau_a(\lambda_i)}{\tau_a(\lambda_j)}=\left(\frac{\lambda_j}{\lambda_i}\right)^n \quad (10)$$

基于气溶胶模型模拟结果，Wang 和 Gordon (1994)提出另一种大气校正参数的计算方法，如式(11)所示，并认为该式对 $\varepsilon(\lambda_i,\lambda_{NIR})$ 与波长的关系描述更为准确。

$$\varepsilon(\lambda_i,\lambda_{NIR})=\frac{\rho_{as}(\lambda_i)}{\rho_{as}(\lambda_{NIR})}=\exp(C(\lambda_{NIR}-\lambda_i)) \quad (11)$$

式中，C 与式(10)中的 n 相似，对于同一种气溶胶模型，其值为常数。

清洁水体像元在 NIR 和 SWIR 波段由于其自身强吸收，离水反射率近似为 0，则去瑞利散射反射率 $\rho_c(\lambda)$ 即为该波段处气溶胶反射率，再由 NIR 和 SWIR 波段的气溶胶散射反射率确定研究区域的大气校正参数 $\varepsilon(\lambda_i,\lambda_{NIR})$，结合式(10)或式(11)，以及式(6)即可外推计算得到各个波段的离水反射率。由于太湖湖泊面积为 2427.8 km^2，面积较大，导致其气溶胶的空间分布不一定均匀，简单的选取单一暗像元确定湖泊上方气溶胶模型势必会造成一定误差，因此，在清洁像元选取上还需要要做进一步改进。

3.2 针对 MERIS 数据改进的大气校正算法

针对 MERIS 数据而言，其波段设置并不包括 SWIR 波段，因此如何确定研究区的气溶胶模型成了研究重点。MERIS 数据设有两个常规的大气校正 NIR 波段(778 nm 和 865 nm)，但对于研究区浑浊水体而言，其 NIR 波段离水反射率为 0 的假设不能成立；而 761 nm 和 900 nm 波段分别位于氧气和水汽吸收带，使得这两个波段的离水反射率较接近于 0，对于较清洁像元，其离水反射率可近似为 0，因此设想通过这两个波段改进传统的 NIR 算法。

3.2.1 MERIS Level 2p 辅助的暗像元选取

MERIS Level 2p 数据是在 MERIS Level 1p 数据的基础上进行大气校正得到的，其大气校正的过程如下：首先，假设一个总悬浮颗粒物浓度的初始值，通过查找表得到其近红外波段的离水反射率；然后，结合近红外波段离水反射率与水体固有光学特性之间的关系，利用 Gordon 大气校正方法迭代优化进行大气校正(Moore 等, 1999)。该方法在光学特性主要由浮游植物及其伴生物决定的一类水体以及悬浮物、CDOM 浓度较低的近岸二类水体中应用效果较好，但在内陆混浊二类水体中仍有一定的不适用性(黄昌春, 2011)，可见光短波波段常出现过校正现象，即校正结果的离水反射率小于 0 值，仅在水体浑浊度较低的湖区，存在少部分区域其校正结果为正值。

与海洋近岸二类水体相比，太湖水体组分复杂，大部分区域浑浊度较高，含藻类水体光学特性被高浓度的悬浮物以及 CDOM 光学特性所掩盖，如图 2 所示为 2007-11-11 太湖的真彩色影像，中部以及西南部水体呈黄褐色，悬浮物浓度较高；而在东太湖、竺山湾、贡湖湾以及胥口湾附近水色呈蓝绿色，表明这些区域的水体悬浮物浓度较低。调查结果表明，东部湖区含有大量的水草，水体相对清洁，这与该区域水体呈蓝绿色是一致的。

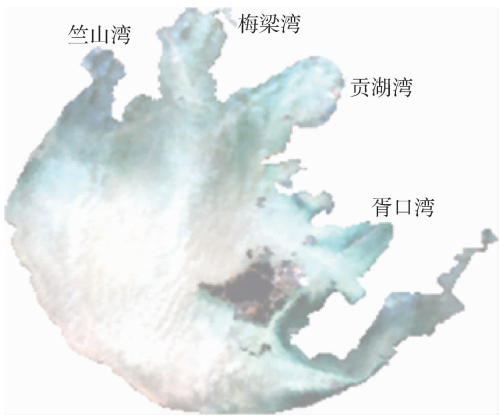

图 2 2007-11-11 MERIS Level 1p 第 6、第 4、第 2 波段真彩色合成影像

如图 3 所示，2007-11-11 在可见光短波波段校正后离水反射率值大于 0 的点(深色区域)较少，多分布在东太湖和胥口湾，在竺山湾和贡湖湾入口也有零星分布，MERIS 数据的大气校正算法在这些点校正成功，即可认为这些点的水体为相对较清洁水体，这与图 2 中太湖水体真彩色合成中所反映的信息相一致，可用于后续的暗像元选取。

为了克服单一暗像元以局部的大气状况来代替整体的大气状况而产生的误差，选取多暗像元进行大气校正(齐志新和邓孺孺, 2007；陈军 等, 2011)。暗像元尽量在 MERIS Level 2p 412 nm 波段离水反射率大于 0 的像元中按区域分布均匀选取，以保证

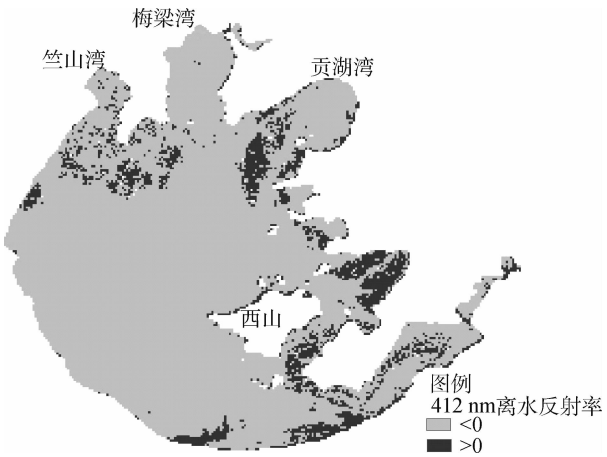

图 3 2007-11-11 MERIS Level 2p 影像
412 nm 波段离水反射率值

下文中大气校正参数计算具有区域的代表性。本文中每幅 MERIS Level 2p 影像选取 30 个暗像元点,提取其坐标信息,再在 MERIS Level 1p 影像中提取对应坐标点的反射率信息,以供后续大气校正参数 $\varepsilon(\lambda_i,\lambda_{NIR})$ 的计算。

3.2.2 大气校正波段选取

太湖浑浊水体组分复杂,使用 MERIS 常规大气校正波段(778 nm 和 865 nm)会造成较大的误差,而 MERIS 761 nm 和 900 nm 波段分别位于氧气和水汽吸收带,一般用于氧气和水汽柱的反演,不常用于大气校正。但正是由于氧气和水汽的吸收,使得 761 nm 和 900 nm 波段的大气透过率 $t(\lambda)$ 很小,在标准的中纬度夏季大气模型下,其透过率只有 13% (Liang, 2004); 同时,收集的 MERIS Level 1p 数据显示,较清洁像元在 761 nm 和 900 nm 波段其反射率值在 0.01—0.03,远小于其他可见光波段传感器接收到的反射率值。由于 $t(\lambda)$ 和 $\rho_w(\lambda)$ 值都较小,传感器接收到的水体反射率透过大气之后的信息 $t(\lambda)\cdot\rho_w(\lambda)$ 趋近于 0,故传感器接收到的信息几乎全部来自于大气分子散射以及气溶胶粒子的散射,这是选用这两个波段来计算大气校正参数的理论基础。

3.2.3 大气校正参数 $\varepsilon(\lambda_i,\lambda_{NIR})$ 的计算

2.1 节中介绍了两种单次散射条件下计算大气校正参数 $\varepsilon(\lambda_i,\lambda_{NIR})$ 的方法,一种是波段比值的幂函数,另一种是波长之差的指数函数,在考虑多次散射的情况下,下文利用 6S 辐射传输模型模拟数据对这两种计算方法适用性,及精度进行比较分析。

6S 模型是目前世界上发展得比较完善的大气校正模型之一,它通过模拟太阳辐射在大气中的传输状况而进行大气校正(Vermote 等, 1997a)。本文利用 6S 辐射传输方程模拟了 5 种气溶胶模型(生物质燃烧型、大陆型、海洋型、平流层型、城市型)(Vermote 等, 1997b)在太阳天顶角 60°、卫星天顶角 45°、相对方位角 90°、能见度 22 km 的条件下各波长的气溶胶多次散射值,大气校正参数 $\varepsilon(\lambda_i,900)$ 为各波长气溶胶多次散射与 900 nm 波长处气溶胶多次散射之比。为了直观比较两种表达式(式(10)(11))对 $\varepsilon(\lambda_i,900)$ 与波长 λ_i 关系的描述,如图 4 所示。

由图 4 可知,折线的斜率即分别为式(10)、式(11)中的 n 和 C,对于同一种气溶胶模型其值为常数。图 4(a)中,城市型气溶胶模型下,$\ln(\varepsilon(\lambda_i,900))$ 与 $\ln(900/\lambda_i)$ 的线性关系明显,而在其他几种气溶胶模型下,斜率随着 $\ln(900/\lambda_i)$ 的增加而减小; 而图 4(b)中的线性关系较图 4(a)更为明显。为了比较两种计算方法的线性拟合精度,表 1 列出了线性拟合的斜率以及 R^2。

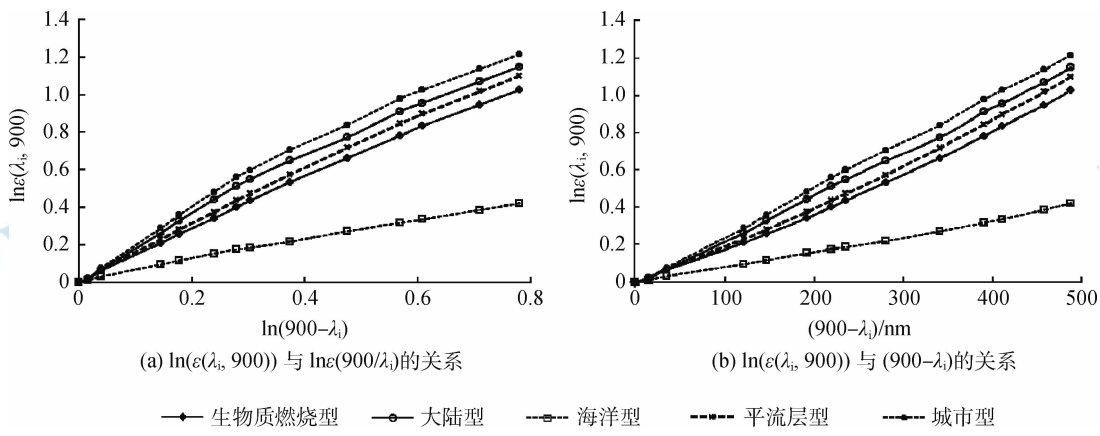

(a) $\ln(\varepsilon(\lambda_i,900))$ 与 $\ln\varepsilon(900/\lambda_i)$ 的关系
(b) $\ln(\varepsilon(\lambda_i,900))$ 与 $(900-\lambda_i)$ 的关系

图 4 5 种气溶胶模型的 $\varepsilon(\lambda_i,900)$ 与波长关系

表 1　5 种气溶胶模型的两种大气校正参数表达式下的拟合结果

气溶胶模型	$\ln(\varepsilon(\lambda_i,\lambda_j))=n\ln\left(\frac{\lambda_j}{\lambda_i}\right)$		$\ln(\varepsilon(\lambda_i,\lambda_j))=C(\lambda_j-\lambda_i)$	
	斜率 n	R^2	斜率 C	R^2
生物质燃烧型	1.5858	0.9856	0.0025	0.9995
大陆型	1.4942	0.9894	0.0024	0.9995
海洋型	1.4296	0.9976	0.0023	0.9961
平流层型	1.3321	0.9981	0.0021	0.9953
城市型	0.5338	0.9961	0.0008	0.9967

由表 1 可知，两种计算大气校正参数 ε 的方法都能较好地表达大气校正参数与波长之间的关系，线性拟合的精度 R^2 都在 0.985 以上；但相比较而言，式(11)在各种气溶胶模型下表现更为稳定，精度都在 0.995 以上；而式(10)的稳定性稍差，在大陆型以及生物质燃烧型气溶胶模型下 R^2 低于 0.99。$\ln(\varepsilon(\lambda_i,900))$ 与 $(900-\lambda_i)$ 的线性关系更加明显，这与 Wang 等人的研究结果一致(Wang 和 Gordon, 1994)，故而本文采取该种计算方法来计算各波段大气校正参数 $\varepsilon(\lambda_i,\lambda_{NIR})$，如式(12)所示。

$$\varepsilon(\lambda_i,\lambda_{NIR})=\frac{\rho_A(\lambda_i)}{\rho_A(\lambda_{NIR})}=\exp(C(\lambda_{NIR}-\lambda_i)) \quad (12)$$

式中，ρ_A 为气溶胶多次散射反射率，由此得到各波段大气校正参数 $\varepsilon(\lambda_i,\lambda_{900})$，再根据式(12)得到各波段的气溶胶散射；最后结合式(5)(6)计算得到各波段的水体离水反射率。

4　结果和讨论

为了检验本文所用的基于氧气和水汽吸收波段的暗像元假设的大气校正算法的精度，对该算法校正结果与准同步样点实测离水反射率进行了对比；同时，将该算法与其他几种常用的大气校正算法校正结果进行比较。

用于精度验证的评判标准主要有：均方根百分比 RMSP (Root Mean Square of Percentage)、相对误差 RE (Relative Error)以及均方根误差 RMSE(Root Mean Square error)。其中 RMSE 与 RE 的定义表达式不再赘述(黄昌春, 2011)，RMSP 的定义如下：

$$\mathrm{RMSP}=\frac{\sqrt{\sum_{i=1}^{n}\left(\frac{V_{\mathrm{estimated}-i}-V_{\mathrm{measured}-i}}{V_{\mathrm{measured}-i}}\right)^2}}{n}100\% \quad (13)$$

式中，$V_{\mathrm{estimated}-i}$ 为估算值，$V_{\mathrm{measured}-i}$ 为测量值，n 为样本数。

4.1　与实测数据的对比

利用上述方法，对 2007-11-11、2008-11-20、2009-04-25 3 天的 MERIS 影像进行大气校正，并选取与传感器过境时间最接近的两个样点的校正结果与实测反射率相比较，结果如图 5 所示。

由图 5 可以看到，2007 年两个准同步样点校正后的光谱曲线与实测光谱曲线形状相似，560 nm 处由于叶绿素和胡萝卜素的弱吸收而造成的反射峰，708 nm 处由含藻类水体的拉曼散射效应而形成的反射峰(李云梅 等, 2006)，以及在 681 nm 处由于叶绿素 a 在红光波段的强吸收所导致的反射谷均出现在校正后的光谱曲线中，说明光谱信息总体保存较好；2008 年准同步样点位于太湖湖心区，2009 年准同步样点位于太湖西部地区。太湖为典型的浅水湖泊，平均水深只有 1.9 m(水深分布见图 1)，湖心区由于水面开阔，风的吹程较长，同样的风速在湖心区作用于湖底的切应力要高于湖湾和沿岸带，再加上其年平均风速要比湖岸大 0.5—1 m/s，在风浪的作用下底泥容易发生再悬浮，致使水体中悬浮物浓度较高(孙顺才和黄漪平, 1993；张运林等, 2006)；西部湖区一方面由于入湖径流携带了大量的悬浮颗粒物进入湖体，另一方面因为此处水域开阔，易受到风浪的影响，造成西部湖区悬浮物浓度较高(孙德勇 等, 2008)，掩盖了色素颗粒物在 675 nm 处的吸收谷和 708 nm 左右的荧光峰，故而光谱比较平缓(Lu 等, 2012；李素菊和王学军, 2003；乐成峰等, 2008)，而校正后的离水反射率也较好地体现了实测光谱的曲线形状，说明该校正方法在浑浊水体以及含藻类水体中都具有一定的适用性。

表 2 列出了 2007 年—2009 年 3 幅 MERIS 影像各波段大气校正精度的评价参数。2007-11-11，5 个采样点 MERIS 各波段的平均相对误差 ARE 基本上都在 0.45 以下，只有第 14 波段(885 nm)校正的相对误差较高，为 0.7231，校正效果最好的波段为第 6 波段(620 nm)，ARE 仅为 0.0134；2008-11-20，6 个采样点 ARE 除了第 1、14 波段，都在 0.4 以下，且均方根百分比都小于 20%；2009-04-25 的校正效果也可以通过这几个参数看到，第 10 波段的 ARE 大于 0.4，其他波段都小于该值，而 RMSP 都在 25% 以下，校正精度较高。总体上而言，MERIS 第 3—第 9 波段的校正精度较高，而蓝光波段(412 nm、443 nm)和近红外波段(754—885 nm)校正精度相对稍差。这可能是由于内陆浑浊水体中含有叶绿素和黄色物质在蓝光波段强吸收作用，导致蓝光水体反射率较低，同时，在蓝光波段大气瑞利散射以及气溶胶

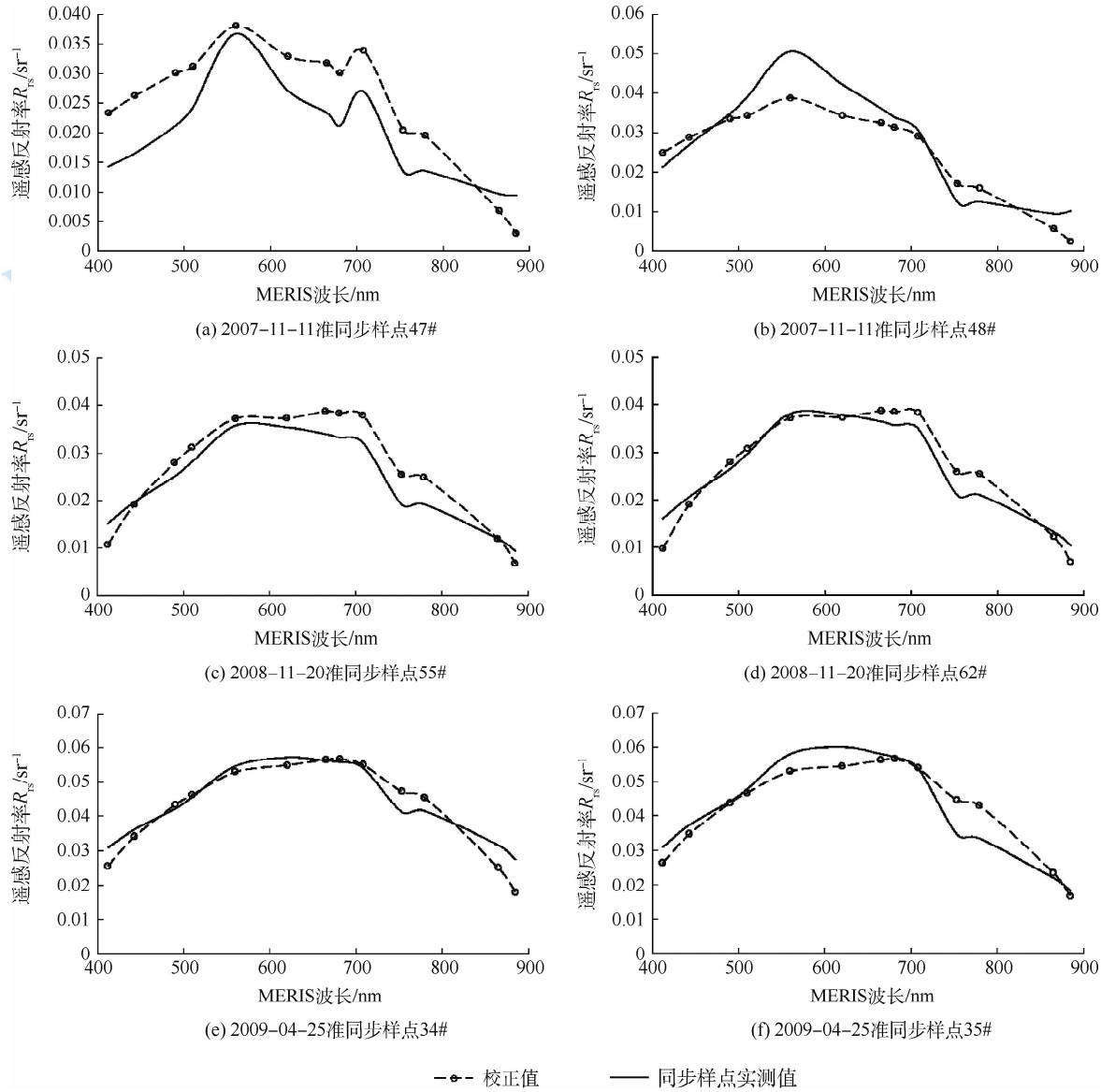

图 5 2007 年—2009 年准同步实测样点大气校正结果

表 2 改进的 Gordon 算法校正结果精度评价

MERIS 波段	中心波长/nm	2007-11-11			2008-11-20			2009-04-25		
		ARE	RMSP/%	RMSE	ARE	RMSP/%	RMSE	ARE	RMSP/%	RMSE
1	412	0.4011	27.53	0.0050	0.4116	16.42	0.0068	0.0088	10.94	0.0058
2	443	0.3257	26.26	0.0056	0.1613	8.60	0.0047	0.0908	10.66	0.0057
3	490	0.1870	17.23	0.0055	0.0269	5.81	0.0039	0.1333	10.44	0.0063
4	510	0.0799	11.72	0.0050	0.0424	5.57	0.0041	0.1042	9.07	0.0063
5	560	0.0997	4.69	0.0044	0.1263	6.93	0.0064	0.0271	6.57	0.0065
6	620	0.0134	9.26	0.0051	0.0725	4.97	0.0047	0.0404	7.50	0.0076
7	665	0.1276	15.80	0.0059	0.0228	4.40	0.0048	0.1146	9.71	0.0083
8	681	0.1696	18.66	0.0060	0.0509	4.82	0.0050	0.1355	10.40	0.0085
9	708	0.1040	14.88	0.0063	0.0002	6.15	0.0077	0.1208	9.61	0.0079
10	754	0.4473	40.90	0.0052	0.1659	11.64	0.0074	0.4199	22.81	0.0096
12	779	0.3527	36.19	0.0048	0.1441	11.00	0.0074	0.3623	20.55	0.0092
13	865	0.3545	13.54	0.0016	0.0886	10.12	0.0064	0.1066	16.69	0.0089
14	885	0.7231	27.05	0.0031	0.3245	14.64	0.0068	0.0426	15.87	0.0098
均值	—	0.2604	20.29	0.0049	0.1260	8.54	0.0059	0.1313	12.37	0.0077

散射强烈，使得水体信号占传感器接收到的信号的比例很小，较小的校正偏差就可以造成较大的相对误差(许华 等, 2011)；另外近红外波段整体信号较弱，也影响了校正精度(周立国 等, 2011)。

4.2 与其他几种二类水体大气校正方法的比较

为了评价本文所述方法的效果，将本文的算法结果与 6S 大气校正方法、黄昌春提出的改进暗像元法以及 Beam C2R 算法结果进行比较。其中，6S 大气校正需要大量的同步气象数据辅助才能得到较为精确的校正效果。本文采用收集到的同步太湖区域 AERONET 数据，计算得到该区域的气溶胶厚度，2007-11-11、2008-11-20、2009-04-25 气溶胶厚度分别为 0.553、0.3429、1.031，将其作为输入参数，辅助进行 6S 大气校正，得到的效果要好于默认能见度 15 km(气溶胶厚度 0.315)进行校正的结果。改进暗像元法，在 MERIS Level 2p 数据中选择混浊度较小的样点作为暗像元，获取其各波段遥感反射率，即离水反射率；再由 MERIS Level 1p 数据得到暗像元点各波段大气层顶部反射率，减去相对应的离水反射率，得到各波段的程辐射值；对获得的多个样点的大气程辐射进行平均处理，利用平均处理后的大气程辐射对整个太湖地区 MERIS Level 1p 产品进行大气校正(黄昌春, 2011)。Beam C2R 方法为 MERIS 影像专业处理软件 Beam 4.8 中嵌入的二类水体大气校正算法，该算法建立在神经网络模型的基础上实现二类水体的大气校正(Doerffer 和 Schiller, 2008)。

4 种大气校正方法与准同步样点实测遥感反射率比较如图 6。

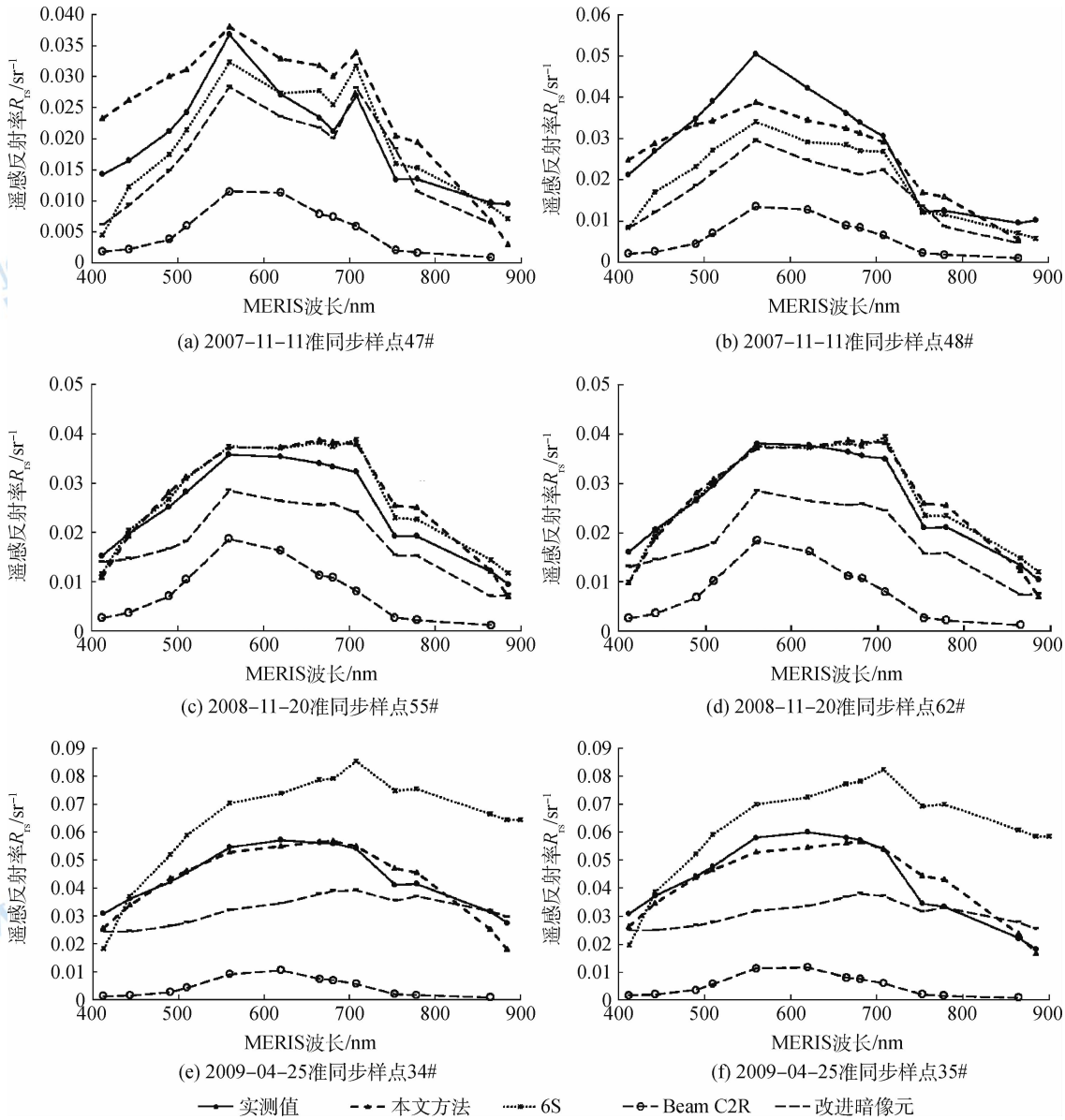

图 6 2007 年—2009 年几种大气校正算法校正结果比较

如图 6 所示,2007 年准同步样点中本文方法与实测离水反射率的曲线最为接近,2007 年以及 2008 年气溶胶辅助 6S 校正的结果也较好,但 2009 年气溶胶辅助的 6S 大气校正结果较实测值偏大,校正效果较差,这可能是由于 2009-04-25 这天 MERIS 影像太湖区域上有薄云,从而影响了大气校正的精度。而改进的暗像元法在 2007 年校正精度较高,曲线整体趋势与实测光谱较为接近,整体稍低于实测值; 但在 2008 年和 2009 年,该方法校正效果稍逊于前两种方法,虽然曲线形状与实测光谱曲线相似,但整体向下偏移,误差稍大;4 种方法中 Beam 自带的 C2R 方法校正效果最差,校正后的值普遍偏低,离水反射率最大值在 0.01 附近徘徊,这可能是由于该方法中使用的大气校正神经网络的训练集样本采用的是欧洲二类水体(Doerffer 和 Schiller, 2008),与中国内陆湖泊水体,如太湖水体光学性质有很大差异,使得该大气校正神经网络不适用于太湖区域,从而造成其校正结果都普遍较低。

为了定量比较 4 种大气方法校正效果,对 4 种方法的大气校正精度评价参数在 14 个波段取均值(其中平均相对误差 ARE 是取绝对值后再平均),得到 2007 年—2009 年 3 幅 MERIS 影像 4 种大气校正的精度参数比较表(表 3)。

表 3 4 种方法大气校正精度比较

大气校正方法	2007-11-11			2008-11-20			2009-04-25		
	ARE	RMSP/%	RMSE	ARE	RMSP/%	RMSE	ARE	RMSP/%	RMSE
本文方法	0.2604	20.2863	0.0049	0.1260	8.5442	0.0059	0.1313	12.3701	0.0077
6S	0.1880	15.8923	0.0052	0.0729	7.7334	0.0060	0.5569	31.4296	0.0111
改进暗像元	0.2808	15.7284	0.0053	0.3703	14.7905	0.0081	0.3944	21.7756	0.0124
Beam C2R	0.7945	31.3332	0.0089	0.7573	28.6722	0.0122	0.8968	44.8558	0.0204

由表 3 可知,2007 年和 2008 年本文所使用的大气校正算法平均相对误差 ARE 略大于 6S 方法,分别为 0.2604 和 0.126,这可能是由于有实测同步 AERONET 气溶胶厚度数据辅助的 6S 算法可以达到较高的校正精度; 2009 年本文方法 ARE 最小,为 0.1313,比气溶胶辅助 6S 校正平均相对误差小二倍以上,也远小于其他两种算法。2007 年—2009 年本文方法的 RMSP 分别为 20.29%、8.54%、12.37%,校正精度平均能达到 80%; 由图 1 中 2007 年—2009 年采样点分布可知,2007 年采样点分布在贡湖湾附近,而 2008 年、2009 年采样点分布于太湖湖心以及西太湖区域,2007-11-11 采样点平均相对误差 ARE 和 RMSP 都明显高于 2008-11-20 以及 2009-04-25,说明本文所用大气校正方法在浑浊水体中应用精度较高,而对浮游藻类主导光学特性的悬浮物浓度较低水体中应用精度有所下降,但精度也能达到 80% 左右。2007 年—2009 年 RMSE 的大小顺序为: 本文算法<气溶胶辅助 6S<改进暗像元<Beam C2R,本文算法的 RMSE 分别为 0.0049、0.0059、0.0077,说明该算法对当天采样点校正精度的稳定性较高,具有一定的适用性。

5 结 论

(1)本文选取了 MERIS 761 nm 和 900 nm 两个氧气和水汽吸收波段来代替传统的大气校正窗口,使得离水反射率接近于 0 的假设得以近似成立,从而改进了传统的近红外波段算法来进行大气校正。校正后的离水反射率光谱也较好的体现了同步样点实测光谱的曲线形状,第 3—9 波段的校正精度较高。

(2)与 6S、改进暗像元以及 Beam C2R 大气校正方法相比而言,气溶胶辅助的 6S 大气校正效果在无云天晴的情况下,校正精度较高,但获取同步的气溶胶数据较难实现; 改进的暗像元法操作简单,校正结果也可以保证一定的精度,但要进一步提高其精度较困难; Beam 自带的 C2R 方法校正效果最差,不适于太湖水体的大气校正; 本文大气校正方法不需要同步实测气溶胶数据,校正精度较高,模型稳定性较强。2007 年—2009 年 3 次准同步实验数据检验表明,其精度可保证在 80% 左右,具有一定的适用性。

(3)本文方法大气校正参数 $\varepsilon(\lambda_i,\lambda_{NIR})$ 的确定是通过多暗像元的选取,并计算各暗像元点的大气校正参数均值作为太湖研究区的统一大气校正参数,虽然减小了单一暗像元计算的误差,但同时也平滑了太湖区域的气溶胶差异,下一步的研究可以考虑从气溶胶分区计算上提高该算法的校正精度。

参考文献(References)

Ångström A. 1964. The parameters of atmospheric turbidity. Tellus, 16(1): 64-75 [DOI: 10.1111/j.2153-3490.1964.tb00144.x]

Bourg L, D'Alba L and Colagrande P. 2008. Meris smile effect characterization and correction [J/OL]. http://earth.eo.esa.int/pcs/envisat/meris/documentation/MERIS_Smile_Effect.pdf

陈军, 孙记红, 付军. 2011. 基于分区暗像元和 Spline 插值方法估算太湖气溶胶光学厚度. 遥感信息, (3): 33-37

陈芸芝, 汪小钦, 高中灵. 2008. 台湾海峡 MERIS 数据大气校正研究. 海洋科学, 32(3): 62-67

Doerffer R and Schiller H. 2008. MERIS Regional Coastal and Lake Case 2 Water Project Atmospheric Correction ATBD. Version 1. 0

Gordon H R, Brown J W and Evans R H. 1988. Exact Rayleigh scattering calculations for use with the Nimbus-7 Coastal Zone Color Scanner. Applied Optics, 27(5): 862-871 [DOI: 10.1364/AO.27.000862]

Gordon H R and Wang M H. 1994a. Retrieval of water-leaving radiance and aerosol optical thickness over the oceans with SeaWiFS: a preliminary algorithm. Applied Optics, 33(3): 443-452 [http://www.ncbi.nlm.nih.gov/pubmed/20862036]

Gordon H R and Wang M H. 1994b. Influence of oceanic whitecaps on atmospheric correction of ocean-color sensors. Applied Optics, 33(33): 7754-7763 [http://www.ncbi.nlm.nih.gov/pubmed/20962986]

Gould R W Jr, Arnone R A and Martinolich P M. 1999. Spectral dependence of the scattering coefficient in case 1 and case 2 waters. Applied Optics, 38(12): 2377-2383 [DOI: 10.1364/AO.38.002377]

He X Q, Pan D L, Bai Y, Zhu Q K and Gong F. 2007. Vector radiative transfer numerical model of coupled ocean-atmosphere system using matrix-operator method. Science in China Series D: Earth Sciences, 50(3): 442-452 [DOI: 10.1007/s11430-007-2075-4]

Hu C M, Carder K L and Muller-Karger F E. 2007. Atmospheric correction of SeaWiFS imagery over turbid coastal waters: a practical method. Remote Sensing of Environment, 74(2): 195-206 [DOI: 10.1016/S0034-4257(00)00080-8]

Huot J P, Tait H, Rast M, Delwart S, Bézy J L and Levrin G. 2001. The optical imaging instruments and their applications: AATSR and MERIS. ESA Bulletin, 106: 56-66

黄昌春. 2011. 顾及颗粒物垂直分布的太湖水体组分生物光学模型反演研究. 南京: 南京师范大学, 79-80

Kuchinke C P, Gordon H R and Franz B A. 2009. Spectral optimization for constituent retrieval in case 2 waters I: implementation and performance. Remote Sensing of Environment, 113(3): 571-587 [DOI: 10.1016/j.rse.2008.11.001]

乐成峰, 李云梅, 查勇, 孙德勇, 王莉珍. 2008. 太湖悬浮物对水体生态环境的影响及其高光谱反演. 环境科学学报, 28(10): 2148-2155

李素菊, 王学军. 2003. 巢湖水体悬浮物含量与光谱反射率的关系. 城市环境与城市生态, 16(6): 66-68

李云梅, 王桥, 黄家柱, 吕恒, 韦玉春. 2006. 用分析模型方法反演水体叶绿素的浓度. 遥感学报, 10(2): 169-175

李云梅, 王桥, 黄家柱, 吕恒, 韦玉春. 2010. 太湖水体光学特性及水色遥感. 北京: 科学出版社: 2-3

Liang S L. 2004. Quantitative Remote Sensing of Land Surfaces. New York: Wiley-Interscience: 46-51

Lu C P, Lv H and Li Y M. 2012. Backscattering properties and parametric model of Taihu Lakebased on spectral classification. Journal of Remote Sensing, 16(2): 419-436

Moore G F, Aiken J and Lavender S J. 1999. The atmospheric correction of water colour and the quantitative retrieval of suspended particulate matter in Case II waters: application to MERIS. International Journal of Remote Sensing, 20(9): 1713-1733 [DOI: 10.1080/014311699212434]

齐志新, 邓孺孺. 2007. 多暗像元大气校正方法. 国土资源遥感, 72(2): 16-19

Ruddick K G, Ovidio F and Rijkeboer M. 2000. Atmospheric correction of SeaWiFS imagery for turbid coastal and inland waters. Applied Optics, 39(6): 897-912 [DOI: 10.1364/AO.39.000897]

Siegel D A, Wang M H, Maritorena S and Robinson W. 2000. Atmospheric correction of satellite ocean color imagery: the black pixel assumption. Applied Optics, 39(21): 3582-3591 [DOI: 10.1364/AO.39.003582]

孙德勇, 李云梅, 王桥, 乐成峰, 黄昌春, 伍蓝. 2008. 太湖水体散射特性及其空间分异. 湖泊科学, 20(3): 389-395

孙顺才, 黄漪平. 1993. 太湖. 北京: 海洋出版社: 10-11

唐军武, 田国良, 汪小勇, 王晓梅, 宋庆君. 2004. 水体光谱测量与分析 I: 水面以上测量法. 遥感学报, 8(1): 37-44

Vermote E F, Tanré D, Deuzé J L, Herman M and Morcrette J J. 1997a. Second Simulation of the Satellite Signal in the Solar Spectrum, 6S: An Overview. IEEE Transactions on Geoscience and Remote Sensing, 35(3): 675-686 [DOI: 10.1109/36.581987]

Vermote E F, Tanré D, Deuzé J L, Herman M and Morcrette J J. 1997b. Second Simulation of the Satellite Signal in the Solar Spectrum (6S). 6S User Guide Version 2

Wang M H and Gordon H R. 1994. A simple, moderately accurate, atmospheric correction algorithm for SeaWiFS. Remote Sensing of Environment, 50(3): 231-239 [DOI: 10.1016/0034-4257(94)90073-6]

Wang M H. 2007. Remote sensing of the ocean contributions from ultraviolet to near-infrared using the shortwave infrared bands: simulations. Applied Optics, 46(9): 1535-1547 [DOI: 10.1364/AO.46.001535]

许华, 顾行发, 李正强, 李莉, 陈兴峰. 2011. 基于辐射传输模型的环境一号卫星 CCD 相机的水体大气校正方法研究. 光谱学与光谱分析, 31(10): 2798-2803

杨健洪, 王锦, 赵东至. 2008. 海洋水色遥感大气校正算法研究进展. 海洋环境科学, 27(1): 97-100

张民伟, 唐军武, 丁静. 2008. 水色大气校正算法综述. 海洋技术, 27(3): 110-114

张运林, 冯胜, 马荣华, 刘明亮, 秦伯强. 2008. 太湖秋季真光层深度空间分布及浮游植物初级生产力的估算. 湖泊科学, 20(3): 380-388

张运林, 秦伯强, 胡维平, 王苏民, 陈宇炜, 陈伟民. 2006. 太湖典型湖区真光层深度的时空变化及其生态意义. 中国科学 D 辑: 地球科学, 36(3): 287-296

周立国, 马蔚纯, 顾万花, 怀红燕. 2011. 基于清洁水体像元法的环境-1A 卫星 CCD 水体图像大气校正. 光谱学与光谱分析, 31(8): 2238-2242

Zhu J J, Chen J, Matsushita B, Yang W and Fukushima T. 2012. Atmospheric correction of ENVISAT/MERIS data over case II waters: the use of black pixel assumption in oxygen and water vapour absorption bands. International Journal of Remote Sensing, 33(12): 3713-3732 [DOI: 10.1080/01431161.2011.632656]

遥感学报

启功先生创刊题名

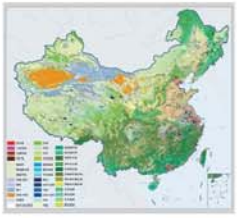

封面说明

About the Cover

2010年中国土地覆被遥感监测数据集（ChinaCover2010）

The China National Land Cover Data for 2010 (ChinaCover2010)

2010年中国土地覆被遥感监测数据集（ChinaCover2010）由中国科学院遥感与数字地球研究所联合其他9个单位历时两年完成，应用30 m空间分辨率的环境星（HJ-1A/1B）数据，利用联合国粮农组织（FAO）的LCCS分类工具，构建了适用于中国生态特征的38类土地覆被分类系统，采用基于超算平台的数据预处理、面向对象的自动分类、地面调查获得的10万个野外样本以及雷达数据辅助分类相结合的方法，数据精度达到85%。ChinaCover2010主要基于国产卫星影像，将遥感与生态紧密结合，充足的野外样点以及严格的产品质量控制在最大程度上保证了数据的精度，可为中国生态环境变化评估以及生态系统碳估算提供基础数据支撑。（网址：http://www.chinacover.org.cn）

The China National Land Cover Data for 2010 (ChinaCover2010) has been completed after two years of team effort by the Institute of Remote Sensing and Digital Earth (RADI), Chinese Academy of Sciences (CAS), together with nine other institutions' participation. The HJ-1A/1B satellite at 30 m resolution is main data source. Based on the landscape features in China, 38 land cover classes have been defined using UN FAO Land Cover Classification System (LCCS). Super computers were used in the data preprocessing. An object-oriented method and a thorough field survey (about 100000 field samples) were used in the land cover classification, with radar imagery as auxiliary data. The overall accuracy of ChinaCover2010 is around 85%. Mainly based on domestic imagery, the products take advantage of various in situ data and strict quality control. ChinaCover2010 is a good dataset for ecological environment change assessment and terrestrial carbon budget studies. (Website: http://www.chinacover.org.cn)

遥感学报

JOURNAL OF REMOTE SENSING

YAOGAN XUEBAO（双月刊　1997年创刊）

第17卷　第4期　2013年7月25日

(Bimonthly, Started in 1997)

Vol.17 No.4 July 25, 2013

主　管	中国科学院	Superintended by	Chinese Academy of Sciences
主　办	中国科学院遥感与数字地球研究所 中国地理学会环境遥感分会	Sponsored by	Institute of Remote Sensing and Digital Earth,CAS The Associate on Environment Remote Sensing of China
主　编	顾行发	Editor-in-Chief	GU Xing-fa
编　辑	《遥感学报》编委会 北京市安外大屯路中国科学院遥感与数字地球研究所 邮编：100101　电话：86-10-64806643 http://www.jors.cn E-mail:jrs@irsa.ac.cn	Edited by	Editorial Board of Journal of Remote Sensing Add: P.O.Box 9718, Beijing 100101, China Tel: 86-10-64806643 http://www.jors.cn E-mail: jrs@irsa.ac.cn
出　版	科学出版社	Published by	Science Press
印刷装订	北京科信印刷有限公司	Printed by	Beijing Kexin Printing Co. Ltd.
总 发 行	科学出版社 北京东黄城根北街16号 邮政编码：100717 电话：86-10-64017032 E-mail:sales_journal@mail.sciencep.com	Distributed by	Science Press Add: 16 Donghuangchenggen North Street, Beijing 100717, China Tel: 86-10-64017032 E-mail: sales_journal@mail.sciencep.com
国外发行	中国国际图书贸易总公司 北京399信箱　邮政编码：100044	Overseas distributed by	China International Book Trading Corporation Add: P.O.Box 399, Beijing 100044, China

中国标准连续出版物号：ISSN 1007-4619 / CN 11-3841/TP

CODEN YXAUAB

国内邮发代号：82-324

国外发行代号：BM 1002

定价：70.00元

ISSN 1007-4619

国内外公开发行